Computational Mechanics (2019) 64:625–644
https://doi.org/10.1007/s00466-019-01673-8

ORIGINAL PAPER

A momentum-consistent stabilization algorithm for Lagrangian particle methods in the thermo-mechanical friction drilling analysis

Xiaofei Pan[1] · C. T. Wu[1] · Wei Hu[1] · Youcai Wu[1]

Received: 7 October 2018 / Accepted: 20 January 2019 / Published online: 12 February 2019

Abstract
This paper introduces a new stabilization algorithm to Lagrangian particle methods for the coupled thermal mechanical analysis in the friction drilling simulation. Different from the conventional penalty method which utilizes a direct smoothing of velocity fields in the weak formulation, the proposed algorithm introduces the smoothed velocity fields through linear momentum equations for stabilization. Particle approximations are used for the discretization of coupled thermal mechanical discrete equations. The coupled system is solved by the explicit and staggered time marching scheme. In comparison to the conventional penalty method which requires at least one extra integration point for stabilization, the proposed algorithm needs only one integration point per particle in computation. The essential features of linear and angular momentum conservations are preserved in the explicit dynamic analysis. A bridging scheme is also developed to couple the particle formulation with finite element formulation for practical industrial applications. Several benchmark tests are performed to examine the effectiveness of this new method. Furthermore, a friction drilling application is studied, and the results are compared with the experimental data.

Keywords Particle formulation · Stabilization · Direct nodal integration (DNI) · Momentum-consistent (MC) · Thermal mechanical

1 Introduction

Manufacturing processes such as friction drilling, flow drill screw and metal cutting involve very complex mechanical and thermal phenomena. For example, friction drilling is a nonconventional drilling process that utilizes the heat generated by friction between the rotating tool and metal workpiece to soften the material and create a hole [1]. Unlike traditional drilling, friction drilling is a chip-less and dry manufacturing method that produces the hole in only one operation without the material removal and lubricants. Friction drilling creates sturdy bushing on thin walled structures such as sheet metal or tubing. Friction drilling can be performed on most metal materials using a high-speed rotating tool made of conical tungsten carbide. Typical applications of friction drilling in automotive industry include seat handle/frame, foot pedal, exhaust part, fuel rail, and among others. A growing interest on the study of friction drilling process has been shown by many automobile factories motivated by the need to reduce manufacturing costs and obtain high quality final products.

Numerical modeling is a necessary tool to understand the material flow, temperatures, stresses and strains which are difficult to measure experimentally during friction drilling [2]. Numerical simulation of friction drilling involves solving a coupled thermo-mechanical system, a task that can turn out to be difficult when considerable deformation and material separation are developed in bushing forming. Since Eulerian representation of a material has difficulty in capturing the free surface flow in the simulation of bushing forming, Lagrangian finite element methods [3] have been favored. While the Lagrangian finite element method (FEM) is used in combination with the r-adaptive re-meshing strategy [4, 5] to handle large deformation problems in similar manufacturing processes such as the friction stir spot welding (FSSW) and the friction stir welding (FSW) [6, 7], modeling material separation in the friction drilling process has always been problematic. This is because the r-adaptive

✉ Xiaofei Pan
xfpan@lstc.com

[1] Computational and Multiscale Mechanics Group, Livermore Software Technology Corporation, 7374 Las Positas Road, Livermore, CA 94551, USA

re-meshing may become unstable or unable to maintain high quality when some or lots elements are deleted using the element erosion technique in mimicking the material separation phenomenon during the forming of the metal bushing.

In comparison to Lagrangian finite element methods, Lagrangian particle methods are advantageous in modeling large deformation and material failure [8–10] problems. Lagrangian particle methods were also found to be very effective on reducing volumetric locking and shear locking in solid and structural analyses [11, 12]. Smoothed Particle Hydrodynamics (SPH) method developed by Gingold and Monaghan [13] and Lucy [14] in late 1970s for astrophysical problems has been considered the earliest Lagrangian particle method. In early 1990s, Libersky and Petschek [15] extended SPH to solid mechanics applications. In spite of its popularity in simulating high-velocity impact/penetration and fluid flow problems [16], SPH has limited success in solid mechanics applications due to several numerical instabilities. Among them, tensile instability [17], spurious zero-energy mode [18] and excessive straining [19] are critical to the simulation and have been the important research topics in the past two decades.

Intensive research work has been carried out to resolve those numerical instabilities. For instance, the introduction of Lagrangian kernel [8, 20] or stress points method [21] has been proven to effectively remove the tension instability in Lagrangian particle methods. The origin of spurious zero-energy mode can be explained by inspecting the system of equations of the particle method. A pioneering approach to circumvent this numerical instability was demonstrated by Beissel and Belytschko [22] using a residual-type stabilization procedure. A variant of this stabilization approach includes the non-residual type of stabilization methods [23, 24], stabilized conforming nodal integration (SCNI) method [25], and variationally consistent integration methods [26]. The problem of excessive straining emerges as a numerical instability in Lagrangian particle methods when the strict use of Lagrangian kernel is no longer applicable in large deformation range. In order to enable the Lagrangian type kernel in large deformation analyses, semi-Lagrangian kernel [27] and adaptive anisotropic Lagrangian kernel [28] have been developed. Nevertheless, very few studies [24, 29] have addressed all numerical issues concurrently and comprehensively.

Smoothed Particle Galerkin (SPG) method motivated by Beissel and Belytschko's residual-type stabilization method [22] is one of the new Lagrangian particle methods developed by Wu et al. [29] to deal with those numerical instabilities. Another new Lagrangian particle method which is based on implicit gradient expansion [30], strain gradient stabilization technique [25] and semi-Lagrangian kernel [27] was proposed by Hillman and Chen [24] to sufficiently control those numerical instabilities in severe deformation analysis. Similar strain gradient stabilization approach was recently considered by Wu et al. [31] to study the friction drilling application without considering the thermal effect. These Lagrangian particle methods share a common feature in augmenting the standard quadratic energy functional by a non-residual term for stabilization. Since the stabilization in those methods is accomplished without the use of the residual of the momentum equation, dependence of artificial control parameters for stabilization can be eliminated.

Modeling material separation in three-dimensional problem is another important research topic for Lagrangian particle methods as well as a desirable feature in industrial applications. However, the extant literature in Lagrangian particle methods gives very few examples [9] in simulating the three-dimensional material separation process. In essence, the development of material separation techniques for Lagrangian particle methods faces formidable challenges in tracing moving discontinuities and in dealing with the interaction of particles affected by the discontinuity. In order to avoid those numerical difficulties and meet the current need in industrial applications, a bond-based failure mechanism inspired by the peridynamics method of Silling et al. [32] was introduced to the SPG method by Wu et al. [29] for the material failure analysis. While these new Lagrangian particle methods were developed for pure structural analysis [33], the application to the coupled thermo-mechanical problem in manufacturing applications remains to be developed.

This paper introduces a new stabilization algorithm for Lagrangian particle method in the analysis of coupled thermo-mechanical problems involving large deformation and material failure. The preset numerical algorithm has shown to preserve the desired conservation properties for linear and angular momentums. The remainder of the paper is organized as follows: The preliminaries and weak formulations for the coupled thermal mechanical problem are given in Sect. 2. In Sect. 3, the particle formulation and semi-discrete equations are provided. Several numerical examples are given in Sect. 4, and conclusions are made in Sect. 5. In "Appendix 1", the momentum consistency of our algorithm is verified, and in "Appendix 2", a bridging technique is proposed for the coupling between finite element method and the proposed method.

2 Preliminaries

The highly coupled and nonlinear system in thermo-mechanical equations for the friction drilling simulation is usually difficult to be solved by the simultaneous time-stepping algorithm. In particular, the large and un-symmetric system in the fully coupled thermo-mechanical equations inevitably involves the convergence problem and is expensive to be solved implicitly in the presence of large deformation, material separation, severe contact conditions and

contact-induced thermal shock. Furthermore, friction drilling is a very quick machining process. Therefore, staggered and explicit time-stepping schemes are considered in this study for the application of interest. In the staggered time-steeping algorithm [34], the thermal mechanical coupled system of equations is partitioned into a thermal phase at fixed configuration, followed by a mechanical phase at constant temperature.

In the thermal phase of the coupled system, the transient heat transfer response is considered in a metal workpiece. Linear dependence of heat flux on the temperature gradient is assumed, and isotropic thermal conductivity is assumed in the analysis. Since the temperature range over which the workpiece is observed in experiments is lower than the melting point, it is presumed that the drilling process does not involve material phase change. It is also presumed that the heat generation is only due to plastic deformation and frictional contact between the drilling tool and workpiece. If the thermal exchange due to surface convection and radiation in the workpiece during the friction drilling are neglected, the standard variational formulation of the thermal energy conservation equation can be written to find the temperature field $\theta(\boldsymbol{X},t) \in \Theta = \left\{\theta \in H^1(\Omega) : \theta = \theta_d \text{ on } \partial\Omega_d\right\}$ such that for arbitrary variation $\delta\theta \in \Theta_0 = \left\{\theta \in H^1(\Omega) : \theta = 0 \text{ on } \partial\Omega_d\right\}$ the following equation is satisfied

$$\begin{aligned}\int_\Omega \rho C_p \dot{\theta}\delta\theta \mathrm{d}\Omega + \int_\Omega \kappa\nabla\theta\cdot\nabla(\delta\theta)\mathrm{d}\Omega \\ = \int_{\partial\Omega_n} q_n\delta\theta \mathrm{d}s + \int_\Omega Q\delta\theta\mathrm{d}\Omega + \int_{\partial\Omega_c} h_c\left(\theta_{tool}-\theta\right)\delta\theta\mathrm{d}s \\ + \int_{\partial\Omega_\tau} \beta\boldsymbol{\tau}\cdot\left[\dot{\boldsymbol{u}}^t\right]\delta\theta\mathrm{d}s\end{aligned} \tag{1}$$

In the above equation ρ is the mass density, C_p is the heat capacity, κ is the isotropic thermal conductivity, ∇ is the gradient operator with respect to current position $\boldsymbol{x}$, and $\nabla\cdot$ denotes the divergence operator.$\partial\Omega_d$ describes a Dirichlet boundary imposed by a temperature θ_d, and $\partial\Omega_n$ is the Neumann boundary prescribed by a normal heat flux $q_n = \kappa(\theta)\nabla\theta\cdot\boldsymbol{n}$ where $\boldsymbol{n}$ is the outward unit normal vector. Q denotes the internal heat generation rate per unit deformed volume from plastic deformation and is defined by

$$Q := \eta\boldsymbol{S} : \dot{\boldsymbol{\epsilon}}^p \tag{2}$$

where $\boldsymbol{S}$ and $\dot{\boldsymbol{\epsilon}}^p$ are the deviatoric part of Cauchy stress and the rate of plastic straining, respectively, and η is the Taylor-Quinney [35] coefficient that takes into account the fraction of heat generated by plastic deformation energy dissipation. The boundary $\partial\Omega_c$ denotes the contact surface with a thermal exchange between the tool and work piece. Subsequently, the third term on the right-hand side of (1) designates the interfacial heat transfer where h_c is the heat conductance on $\partial\Omega_c$, and θ_{tool} is the temperature of the tool. The last term on the right-hand side of (1) represents the rate of frictional energy dissipation in which β is the fraction of heat generated by the frictional contact, and $\boldsymbol{\tau}$ is the Cauchy contact traction and $\left[\dot{\boldsymbol{u}}^t\right]$ is the contact slip rate which is regarded as the jump in velocity across the contact surface.

In the mechanical phase, the dynamic process of friction drilling process is described by the equation of motion in the context of large strain analysis. During the friction drilling process, the workpiece experiences different rates of heating and cooling, and thus expansion and contraction. This leads to considerable thermal strains and stresses which need to be taken into account in the mechanical analysis. Using standard procedures, the variational equation for the mechanical problem in friction drilling process is written to find the displacement field $\boldsymbol{u}(\boldsymbol{x},t) \in \boldsymbol{V} = \left\{\boldsymbol{u} \in \boldsymbol{H}^1(\Omega) : \boldsymbol{u} = \boldsymbol{u}_g \text{on} \partial\Omega_g\right\}$, such that for arbitrary variation $\delta\boldsymbol{u} \in \boldsymbol{V}_0 = \left\{\boldsymbol{u} \in \boldsymbol{H}^1(\Omega) : \boldsymbol{u} = 0 \text{on} \partial\Omega_g\right\}$, the following equation is satisfied:

$$\begin{aligned}\int_\Omega \rho\ddot{\boldsymbol{u}}\cdot\delta\boldsymbol{u}\mathrm{d}\Omega + \int_\Omega \delta\boldsymbol{\epsilon}^{\mathrm{T}} : \boldsymbol{\sigma}\mathrm{d}\Omega \\ = \int_\Omega \boldsymbol{b}\cdot\delta\boldsymbol{u}\mathrm{d}\Omega + \int_{\partial\Omega_h} \boldsymbol{h}\cdot\delta\boldsymbol{u}\mathrm{d}s + \int_{\partial\Omega_c} \boldsymbol{\gamma}\cdot\delta\boldsymbol{u}\mathrm{d}s\end{aligned} \tag{3}$$

where $\boldsymbol{b}$ is the body force vector and $\boldsymbol{\sigma}$ is the Cauchy stress obtained from the constitutive law which is temperature dependent. The rate representation of strain field $\dot{\boldsymbol{\epsilon}}$ should consider the thermal effect which is described by

$$\dot{\boldsymbol{\epsilon}} = \dot{\boldsymbol{\epsilon}}^e + \dot{\boldsymbol{\epsilon}}^p + \dot{\boldsymbol{\epsilon}}^\theta \tag{4}$$

where $\dot{\boldsymbol{\epsilon}}^e$ is elastic strain rate tensor, and $\dot{\boldsymbol{\epsilon}}^\theta = \alpha\dot{\theta}\boldsymbol{I}$ is the thermal strain rate tensor with α denoting the thermal expansion coefficient. $\partial\Omega_g$ denotes a Dirichlet boundary imposed by a displacement $\boldsymbol{u}_g$, and $\partial\Omega_h$ is the Neumann boundary prescribed by a surface traction $\boldsymbol{h}$. $\boldsymbol{\gamma}$ denotes the contact traction which is governed by the unilateral contact conditions and Coulomb friction law [3]. Using Eq. (4) and the isothermal assumption from the staggered time-steeping algorithm, the corresponding rate form of the constitutive relation in mechanical phase can be written as

$$\dot{\boldsymbol{\sigma}} = \boldsymbol{C}(\theta) : \left(\dot{\boldsymbol{\epsilon}}^e = \dot{\boldsymbol{\epsilon}} - \dot{\boldsymbol{\epsilon}}^p - \dot{\boldsymbol{\epsilon}}^\theta\right) \tag{5}$$

where $\boldsymbol{C}$ is the temperature-dependent fourth-order isotropic elastic tensor.

Consequently, the thermal mechanical problem in metal drilling process can be stated by coupling the mechanical weak form in Eq. (3) with the thermal weak form in Eq. (1) using the staggered time marching scheme. The coupled system of equations is discretized using meshfree approximations and solved by the classical explicit time-stepping approach which is described in the next section.

3 Momentum consistent smoothing algorithm

3.1 Meshfree approximation and discretization for mechanical analysis

For a particle distribution denoted by an index set $Z_I = \{X_I\}_{I=1}^{NP} \in R^3$, approximating the displacement field using the meshfree approximation gives

$$\boldsymbol{u}^h(\boldsymbol{X},t) = \sum_{I\in Z_I} \phi_I^a(\boldsymbol{X})\boldsymbol{u}(\boldsymbol{X}_I,t) = \sum_{I\in Z_I} \phi_I^a(\boldsymbol{X})\boldsymbol{u}_I(t) \quad \forall \boldsymbol{X}\in\Omega \tag{6}$$

where NP is the total number of particles in the discretization. $\phi_I^a(\boldsymbol{X}), I = 1,\ldots,NP$ can be interpreted as the Lagrangian shape functions of the meshfree approximation for displacement field $\boldsymbol{u}^h$ where the superscript "a" denotes the support size of $\phi_I^a(\boldsymbol{X})$.

It is difficult, if not impossible, to build conforming grid for spatial domain integration of the weak form in Eq. (3) due to material failure and separation in friction drilling processes. Therefore, grid based spatial domain integration such as Gauss quadrature is not applicable for this type of problem. Alternatively, the direct nodal integration (DNI) scheme seems to be a feasible approach. However, the standard DNI scheme for the spatial domain integration of the weak form in Eq. (3) leads to the numerical instability known as the zero-energy mode in structural analysis. To suppress the zero-energy mode and stabilize the solution, stabilization method needs to be introduced in the formulation. Existing stabilization algorithms [26, 28, 29] for Lagrangian particle methods were developed based on the penalty method.

This paper proposes a different stabilization approach for the coupled thermal mechanical problem. Firstly, the mechanical part of the coupling problem is recalled as follows: find $\boldsymbol{u}^h(\boldsymbol{X},t) \in \boldsymbol{V}^h$ such that

$$\begin{aligned}\int_\Omega \rho\ddot{\boldsymbol{u}}^h\cdot\delta\boldsymbol{u}^h\mathrm{d}\Omega + \int_\Omega \boldsymbol{\sigma}\cdot\nabla\delta\boldsymbol{u}^h\mathrm{d}\Omega \\ = \int_\Omega \boldsymbol{b}\cdot\delta\boldsymbol{u}^h\mathrm{d}\Omega + \int_{\partial\Omega_h}\boldsymbol{h}\cdot\delta\boldsymbol{u}^h\mathrm{ds} \\ + \int_{\partial\Omega_c}\boldsymbol{\gamma}\cdot\delta\boldsymbol{u}^h\mathrm{ds} \quad \forall\boldsymbol{u}^h\in\boldsymbol{V}^h\end{aligned} \tag{7}$$

with initial conditions

$$\boldsymbol{u}^h(\boldsymbol{X},0) = \boldsymbol{u}_0(\boldsymbol{X}) \tag{8}$$

$$\dot{\boldsymbol{u}}(\boldsymbol{X},0) = \dot{\boldsymbol{u}}_0(\boldsymbol{X}) \tag{9}$$

It's known that in the explicit Lagrangian formulations such as FEM [3] and RKPM [8], the nodal velocities $\dot{\boldsymbol{u}}(\boldsymbol{X}_I)$, used to update the strain in the current time step are directly taken as the ones from last time step. Whereas in the present formulation these nodal velocities are computed with the aid of a momentum-consistent smoothing algorithm, which starts with the evaluation of the nodal momentum $\boldsymbol{P}_I$ defined in the following discrete smoothing formulation:

$$\underbrace{\boldsymbol{P}_I}_{\text{Nodal momentum}} = \sum_{J\in Z_I}\hat{m}_J\phi_I^a(\boldsymbol{X}_J)\hat{\boldsymbol{u}}_J \tag{10}$$

where $\hat{m}_J$ is the mass occupied by the node J in the DNI scheme, which doesn't change with time, and $\hat{\boldsymbol{u}}_J$ are the unsmoothed nodal value of velocity. Here, $\phi_I^a(\boldsymbol{X})$ is the shape function of node I in Eq. (6) and serves as the smoothing function in Eq. (10). As illustrated in Fig. 1, the support domain node I serves as the integration region to calculate the smoothed nodal momentum for node I. The nodal mass m_I is calculated in a similar way given by:

$$\underbrace{m_I}_{\text{Nodal mass}} = \sum_{J\in Z_I}\hat{m}_J\phi_I^a(\boldsymbol{X}_J) \tag{11}$$

which equals to the value of node J in the diagonally lumped mass matrices in the DNI scheme. Subsequently, the nodal velocity is calculated by

$$\underbrace{\dot{\boldsymbol{u}}_I}_{\text{Nodal velocity}} = \sum_{J\in Z_I}\hat{m}_J\phi_I^a(\boldsymbol{X}_J)\hat{\dot{\boldsymbol{u}}}_J \Big/ \sum_{J\in Z_I}\hat{m}_J\phi_I^a(\boldsymbol{X}_J) \tag{12}$$

It can be verified that the linear and angular moments are consistent before and after smoothing. The verification is shown in "Appendix 1".

With the computed nodal velocity, the strain rate of node J can be obtained by

$$\dot{\boldsymbol{\varepsilon}}_J = \nabla^{\mathrm{S}}\dot{\boldsymbol{u}}_J \tag{13}$$

The corresponding stress increment is updated from the strain increment using the constitutive equations the Eq. (5), and the stress can be calculated by using the stress updating algorithm described in [3].

Consequently, the nodal accelerations can be calculated using the DNI scheme for the mechanical weak form of Eq. (7).

$$\boldsymbol{M}\ddot{\boldsymbol{U}} = \boldsymbol{F}^{\mathrm{ext}} + \boldsymbol{F}^{\mathrm{c}} - \boldsymbol{F}^{\mathrm{int}} \tag{14}$$

where $\boldsymbol{F}^{\mathrm{ext}}$ and $\boldsymbol{F}^{\mathrm{c}}$ are the standard external force matrix and contact force matrix, respectively. The mass matrix $\boldsymbol{M}$ and the internal force $\boldsymbol{F}^{\mathrm{int}}$ are given by

$$\boldsymbol{M}_{IJ} = \sum_{k\in Z_I}\phi_I^a(\boldsymbol{X}_k)\phi_J^a(\boldsymbol{X}_k)\hat{m}_k\boldsymbol{I}_{3\times3} \tag{15}$$

$$\boldsymbol{F}_I^{\mathrm{int}} = \sum_{k\in Z_I}\boldsymbol{B}_I^{\mathrm{T}}(\boldsymbol{X}_k)\boldsymbol{\Xi}(\boldsymbol{X}_k)\hat{m}_k/\rho_k \tag{16}$$

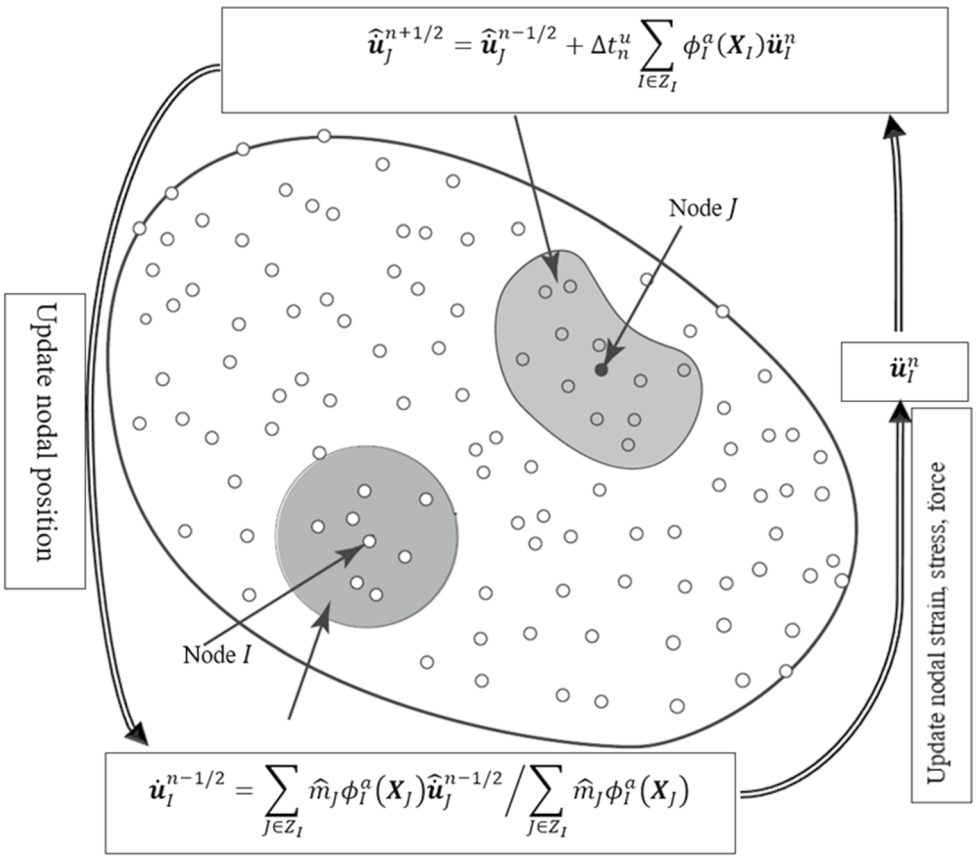

Fig. 1 Illustration of the relationship between the nodal velocities and unsmoothed nodal velocities

where

$$\boldsymbol{B}_I(\boldsymbol{X}_k) = \begin{bmatrix} \phi_{I,x}^a(\boldsymbol{X}_k) & 0 & 0 \\ 0 & \phi_{I,y}^a(\boldsymbol{X}_k) & 0 \\ 0 & 0 & \phi_{I,z}^a(\boldsymbol{X}_k) \\ 0 & \phi_{I,z}^a(\boldsymbol{X}_k) & \phi_{I,y}^a(\boldsymbol{X}_k) \\ \phi_{I,z}^a(\boldsymbol{X}_k) & 0 & \phi_{I,x}^a(\boldsymbol{X}_k) \\ \phi_{I,y}^a(\boldsymbol{X}_k) & \phi_{I,x}^a(\boldsymbol{X}_k) & 0 \end{bmatrix} \tag{17}$$

$$\boldsymbol{\Xi}(\boldsymbol{X}_k) = \left[\sigma_{xx}(\boldsymbol{X}_k)\ \sigma_{yy}(\boldsymbol{X}_k)\ \sigma_{zz}(\boldsymbol{X}_k)\ \sigma_{yz}(\boldsymbol{X}_k)\ \sigma_{xz}(\boldsymbol{X}_k)\ \sigma_{xy}(\boldsymbol{X}_k)\right]^{\mathrm{T}} \tag{18}$$

In Eq. (18), $\sigma_{xx}(\boldsymbol{X}_k)$,$\sigma_{yy}(\boldsymbol{X}_k)$, $\sigma_{zz}(\boldsymbol{X}_k)$, $\sigma_{\boldsymbol{xy}}(\boldsymbol{X}_k)$, $\sigma_{xz}(\boldsymbol{X}_k)$ and $\sigma_{yz}(\boldsymbol{X}_k)$ are the stress components of the node k. ρ_k is the nodal density, and should be updated by

$$\rho_k^{n+1} = \rho_k^n \left[1 - \Delta t_{n+1/2}^u \boldsymbol{\nabla}\cdot\dot{\boldsymbol{u}}_k\right] \tag{19}$$

From Eq. (16), the acceleration can be obtained as

$$\ddot{\boldsymbol{U}}_n = \boldsymbol{M}^{\mathrm{l}^{-1}}\left(\boldsymbol{F}^{\mathrm{ext},n} + \boldsymbol{F}^{\mathrm{c},n} - \boldsymbol{F}^{\mathrm{int},n}\right) \tag{20}$$

where $\boldsymbol{M}^{\mathrm{l}}$ is the lumped mass matrix,

$$\boldsymbol{M}_I^{\mathrm{l}} = \sum_{k\in Z_I} \phi_I^a(\boldsymbol{X}_k)\hat{m}_k \boldsymbol{I}_{3\times 3} \tag{21}$$

Subsequently, the unsmoothed value of nodal velocities should be updated using the nodal accelerations given by:

$$\hat{\boldsymbol{u}}_J^{n+1/2} = \hat{\boldsymbol{u}}_J^{n-1/2} + \Delta t_n^u \sum_{I\in Z_I} \phi_I^a(\boldsymbol{X}_J)\ddot{\boldsymbol{u}}_I^n \tag{22}$$

where $\Delta t_n^u = t_{n+1/2}^u - t_{n-1/2}^u$, $t_{n+1/2}^u = \left(t_{n+1}^u + t_n^u\right)/2$. These velocities are used to calculate the nodal velocities by using the momentum-consistent smoothing algorithm in the next time step. Now the relationship between the nodal velocities and unsmoothed nodal velocities is shown in Fig. 1.

In the present formulation, the central difference scheme is used for temporal integration. The nodal displacement from time t_n to t_{n+1} can be calculated by using the central difference integration algorithm:

$$\boldsymbol{U}_{n+1} = \Delta t_{n+1/2}^u \dot{\boldsymbol{U}}^{*,n+1/2} \tag{23}$$

where $\Delta t_{n+1/2}^u = t_{n+1}^u - t_n^u$, while the updated nodal velocity to be calculated by:

$$\dot{\boldsymbol{U}}^{*,n+1/2} = \dot{\boldsymbol{U}}^{n-1/2} + \Delta t_n^u \ddot{\boldsymbol{U}}^n \tag{24}$$

Accordingly, the new positions of the nodes or particles are updated using the displacement approximation, that is

$$\boldsymbol{x}_I^{n+1} = \boldsymbol{x}_I^n + \sum_{J\in Z_I} \phi_J^a(\boldsymbol{X}_I)\boldsymbol{u}_J^{n+1} \tag{25}$$

The present formulation for structural analysis is illustrated in Algorithm 1

Algorithm 1: Present formulation for structural analysis

Initialization: calculate the mass $\hat{m}$ occupied by each node, set nodal velocities

While $t_{n+1}^{u} < t_{\text{end}}$ **do**

  For all i **do**

    Find influencing nodes, construct shape function and calculate its derivatives.

  For all i **do**

    Interpolate nodal values of the temperature field at time t_n^u using the ones from thermal solver at time t_n^θ and t_{n+1}^θ, where $t_n^\theta \le t_n^u \le t_{n+1}^\theta$

    Compute the nodal mass using Eq. (11), and smooth nodal velocity using Eq. (12)

  For all i **do**

    Update nodal strain rate using Eq. (13)

    Update nodal stress rate using Eq. (5) and the corresponding nodal stress.

    Compute internal forces using Eq. (16), external forces and contact forces.

    Update nodal density using Eq. (19)

  For all i **do**

    Compute nodal acceleration using Eq. (20)

    Update nodal velocity using Eq. (24) and nodal displacement using Eq. (23)

    Accumulate the plastic work and frictional work

  For all i **do**

    Update unsmoothed nodal velocity using Eq. (22)

    Update the nodal position using Eq. (25)

3.2 Meshfree approximation and discretization for thermal analysis

In a similar way as structural problem, the standard meshfree Galerkin method [8] for the thermal problem can be formulated on a finite dimensional space $\Theta^h \in \Theta$ employing the thermal weak form of Eq. (1) to find $\theta^h \in \Theta^h$ such that

$$\begin{aligned}\int_\Omega \rho C_p \dot{\theta}^h \delta\theta^h \mathrm{d}\Omega + \int_\Omega \kappa \nabla\theta^h \cdot \nabla\left(\delta\theta^h\right)\mathrm{d}\Omega \\ = \int_{\partial\Omega_n} q_n \delta\theta^h \mathrm{d}s + \int_\Omega Q\delta\theta^h \mathrm{d}\Omega + \int_{\partial\Omega_c} h_c\left(\theta_{\text{tool}} - \theta^h\right)\delta\theta^h \mathrm{d}s \\ + \int_{\partial\Omega_\tau} \beta\boldsymbol{\tau}\cdot\left[\dot{\boldsymbol{u}}^{\mathrm{t}}\right]\delta\theta^h \mathrm{d}s \quad \forall\delta\theta^h \in \Theta_0^h \end{aligned} \tag{26}$$

with initial condition

$$\theta^h(\boldsymbol{X},0) = \theta_0(\boldsymbol{X}) \text{ in } \Omega \tag{27}$$

where $\Theta^h = span\left\{\phi_I^a : I \in Z_I\right\}$ and Z_I is an index set. $\left\{\phi_I^a\right\}_{I\in Z_I}$ are the meshfree shape functions.

Similar smoothing algorithm is applied to the thermal analysis. At the beginning of every time step, the nodal temperatures are obtained with the following formulation:

$$\theta_I = \sum_{J\in Z_I} \hat{m}_J \phi_I^a\left(\boldsymbol{X}_J\right)\hat{\theta}_J / \sum_{J\in Z_I} \hat{m}_J \phi_I^a\left(\boldsymbol{X}_J\right) \tag{28}$$

with the smoothed nodal temperatures, the space gradient of the temperature $\boldsymbol{\Gamma}(\boldsymbol{X})$ can be computed:

$$\boldsymbol{\Gamma}(X) = \nabla\theta^h = \left[\sum_{J\in Z_I} \phi_{J,x}^a(\boldsymbol{X})\theta_J \sum_{J\in Z_I} \phi_{J,y}^a(\boldsymbol{X})\theta_J \sum_{J\in Z_I} \phi_{J,z}^a\left(\boldsymbol{X}_I\right)\theta_J\right]^{\mathrm{T}} \tag{29}$$

Consequently, the temperature rate can be calculated using the DNI scheme for the thermal weak form of Eq. (27)

$$\boldsymbol{C}\dot{\boldsymbol{\theta}} = \boldsymbol{R}^{\partial\Omega_n} + \boldsymbol{R}^{\partial\Omega_c} + \boldsymbol{R}^{\partial\Omega_\tau} - \boldsymbol{R}^{\Omega} \tag{30}$$

where

$$C_{IJ} = \sum_{k\in Z_I} \phi_I^a\left(\boldsymbol{X}_k\right)\phi_J^a\left(\boldsymbol{X}_k\right)\hat{m}_k C_p\left(\boldsymbol{X}_k\right) \tag{31}$$

$$R_I^{\partial\Omega_n} = \sum_{k\in Z_I} q_n\left(\boldsymbol{X}_k\right)\phi_I^a\left(\boldsymbol{X}_k\right)s\left(\boldsymbol{X}_k\right) \tag{32}$$

$$R_I^{\partial\Omega_c} = \sum_{k\in Z_I} h_c\left[\theta_{\text{tool}} - \theta^h\left(\boldsymbol{X}_k,t\right)\right]\phi_I^a\left(\boldsymbol{X}_k\right)s\left(\boldsymbol{X}_k\right) \tag{33}$$

$$R_I^{\partial\Omega_\tau} = \sum_{k\in Z_I} \beta\boldsymbol{\tau}\left(\boldsymbol{X}_k\right)\cdot\left[\dot{\boldsymbol{u}}^{\mathrm{t}}\left(\boldsymbol{X}_k\right)\right]\phi_I^a\left(\boldsymbol{X}_k\right)s\left(\boldsymbol{X}_k\right) \tag{34}$$

$$\begin{aligned} R_I^{\Omega} = \sum_{k\in Z_I} \kappa\Big[\Gamma_1\left(\boldsymbol{X}_k\right)\phi_{I,x}^a\left(\boldsymbol{X}_k\right) + \Gamma_2\left(\boldsymbol{X}_k\right)\phi_{I,y}^a\left(\boldsymbol{X}_k\right) \\ + \Gamma_3\left(\boldsymbol{X}_k\right)\phi_{I,z}^a\left(\boldsymbol{X}_k\right)\Big]\hat{m}_k/\rho_k - \sum_{k\in Z_I} Q\left(\boldsymbol{X}_k\right)\hat{m}_k/\rho_k \end{aligned} \tag{35}$$

where $\Gamma_1\left(\boldsymbol{X}_k\right)$, $\Gamma_2\left(\boldsymbol{X}_k\right)$ and $\Gamma_3\left(\boldsymbol{X}_k\right)$ are the 1st–3rd components of $\boldsymbol{\Gamma}\left(\boldsymbol{X}_k\right)$, and $s\left(\boldsymbol{X}_k\right)$ is the surface area occupied by node k. Thermal equation in Eq. (30) is marched through

time using the forward difference algorithm [3] which is given by

$$\boldsymbol{\theta}^{n+1} = \boldsymbol{\theta}^{n} + \Delta t^{\theta}\dot{\boldsymbol{\theta}}^{n} \tag{36}$$

$$\dot{\boldsymbol{\theta}}^{n} = \boldsymbol{C}^{l^{-1}}\left(\boldsymbol{R}^{\partial\Omega_n} + \boldsymbol{R}^{\partial\Omega_c} + \boldsymbol{R}^{\partial\Omega_\tau} - \boldsymbol{R}^{\Omega}\right) \tag{37}$$

In general, the critical time step in the explicit thermal analysis is much larger than that in the explicit structural analysis. In present coupled thermo-structural analysis, the staggered time marching scheme is used, and the explicit thermal analysis loop is activated as soon as $t^{\theta}_{n+1} \le t^{u}_{n+1}$.

The present formulation for thermal analysis is illustrated in Algorithm 2.

Algorithm 2: Present formulation for thermal analysis

Initialization: Set initial nodal temperature

While $t^{\theta}_{n+1} < t_{\text{end}}$ **do**

  If $t^{\theta}_{n+1} \le t^{u}_{n+1}$ **then**

    For all i **do**

      Smoothing nodal temperature using Eq. (28)

    For all i **do**

      Compute the space gradient of the temperature using Eq. (29)

    For all i **do**

      Compute the C^{l}_{I}, $R^{\partial\Omega_n}_{I}$, $R^{\partial\Omega_c}_{I}$, $R^{\partial\Omega_\tau}_{I}$ and R^{Ω}_{I} using Eq. (38), Eq. (32)-(35)

    For all i **do**

      Calculate the temperature rate using Eq. (37)

    For all i **do**

      Update the unsmoothed nodal temperature using Eq. (39)

      Update the temperature field by using Eq. (40)

where the thermal capacity matrix $\boldsymbol{C}$ is advantageously replaced by the lumped matrix $\boldsymbol{C}^{l}$ for the explicit analysis.

$$C^{l}_{I} = \sum_{k\in Z_I} \phi^{a}_{I}(\boldsymbol{X}_k)\hat{m}_k C_p(\boldsymbol{X}_k) \tag{38}$$

At the end of the time step, the particle temperature should be updated using the nodal temperature increment with the following formulation:

$$\hat{\theta}^{n+1}_{J} = \hat{\theta}^{n}_{J} + \Delta t^{\theta}\sum_{I\in Z_J} \phi^{a}_{I}(\boldsymbol{X}_I)\dot{\theta}^{n}_{I} \tag{39}$$

and the temperature field is given as

$$\theta^{h}(\boldsymbol{X},t) = \sum_{J\in Z_I} \phi^{a}_{J}(\boldsymbol{X})\left(\theta^{n}_{J} + \Delta t^{\theta}\dot{\theta}^{n}_{J}\right) \tag{40}$$

The critical time step in the explicit method is governed by the Courant–Friedrichs–Lewy (CFL) condition [3] which is given in the following for the thermal and mechanical analysis respectively

$$\Delta t^{\theta} \le S_{\theta c}\min\left(\frac{\rho C_p l^2}{2\kappa}\right) \quad \Delta t^{u} \le S_{uc}\min\left(\frac{l}{C_u}\right) \tag{41}$$

where the sound speed C_u gives the characteristic speed of the medium in mechanical analysis. l is the support size of the kernel function [8] for the particle system. A scaling factor $S_{\theta c} = 0.15, S_{uc} = 0.9$ is used in this study.

4 Numerical example

The present formulation is implemented into the commercial software LS-DYNA® [36]. To verify the accuracy of the present numerical algorithm, three benchmark problems and one practical application are studied. All numerical examples are performed using beta version LS-DYNA. To setup an LS-DYNA particle analysis with the present formulation, the exact same input as for FEM is used except that a different element type is used in the input to activate the particle.

In the present particle formulation, cuboidal support is used for the MLS approximation. The original nodal support size is determined as the maximum coordinate difference in each direction between the particular node and all other nodes in elements containing it based on the original FEM nodal connectivity, and scaled by the normalized dilation parameter with typical value between 1.5 and 1.9. A normalized support size of 1.8 is used for all the numerical examples in this paper.

It is well known that FEM is an efficient algorithm in practical application. To take advantage of this, coupled finite element and particle method simulations are performed for all the numerical examples that are shown in this paper. For the coupling between the FEM and meshfree methods, wave reflection at the interface is always a concern in an explicit solver for a dynamic event. Liu et al. [37, 38] modified the shape function in the transition area for both

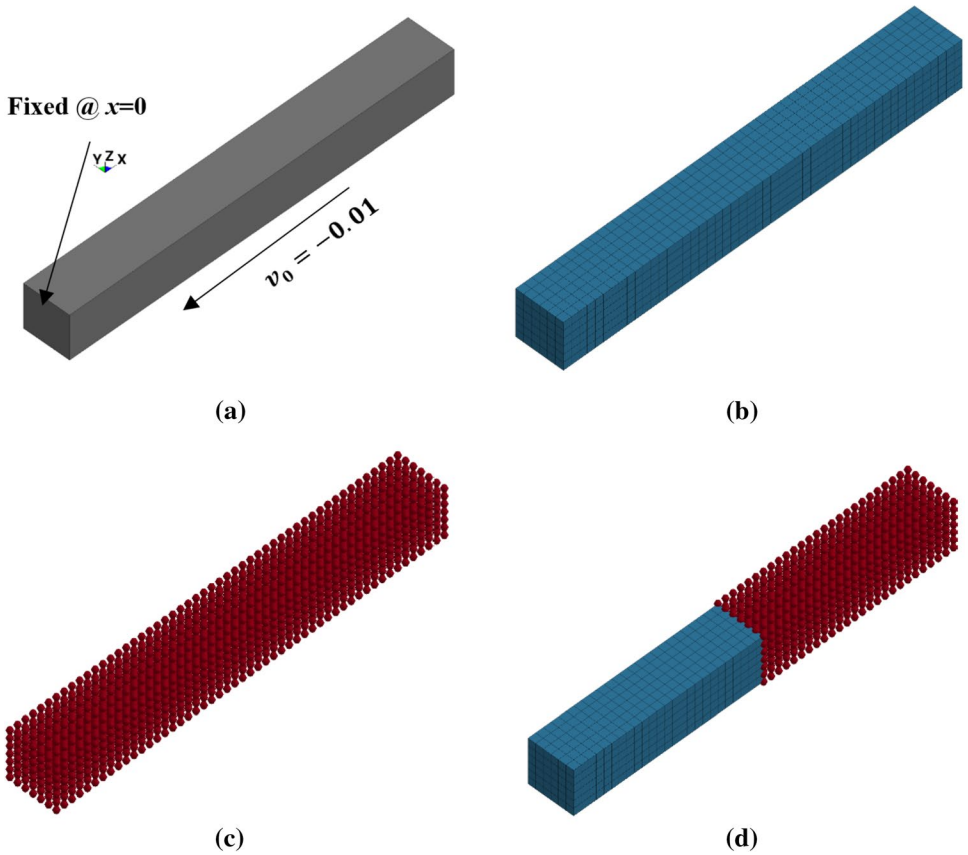

Fig. 2 Geometry and discretization for elastic wave propagation problem: **a** Geometry and boundary condition; **b** FEM model; **c** particle model; **d** coupled model

the reproducing kernel particle method (RKPM) and FEM to couple the RKPM and FEM. Belytschko et al. [39] developed a coupling algorithm for element-free Galerkin (EFG) and FEM by a mixed interpolation in the transition area.

The bridging mechanism for coupling the FEM with the current particle formulation is described in "Appendix 2", and the numerical examples will show that wave reflection issue at the interface is well controlled by using the proposed momentum-consistent algorithm.

4.1 Benchmark tests

Three benchmark tests including a 1D elastic wave propagation, heat conduction and thermal expansion in thin plate and Taylor impact are examined to study the effectiveness of the present formulation.

4.1.1 Elastic wave propagation

This is a fundamental example to test whether the formulation can capture the wave propagation behavior in a dynamic event. The strong form, boundary condition and initial conditions and analytical solution can be referred to [33].

A three-dimensional square rod shown in Fig. 2a is used for the simulation, which has a cross-section of 1.2×1.2, length $L = 10.0$, Young's modulus $E = 100$, Poisson ratio $\nu = 0.0$ and density $\rho = 100.0$. A FEM model, a particle model and a coupled FEM-Particle model shown in Fig. 2b–d are used for comparison, and the nodal spacings in the all directions for all the three models are 0.2.

Figure 3 shows the stress wave profiles at different propagation stages in the whole domain. The black arrow indicates the direction of wave propagation. "CPL" on the legend refers to the coupled model and "Interface" indicates the location of the interface in the coupled model. All the numerical approaches capture the wave propagation behaviors properly compared with the analytical solution. For the coupled model, the incident wave propagates smoothly through the interface at $x = 5$ from FEM zone to particle zone as shown in Fig. 3a, b, and no apparent wave reflection is observed at the interface. The incident wave is reflected at the free end as can be deduced from Fig. 3c, d. Later, the reflected wave propagates smoothly again across the interface from particle zone to FEM zone as shown in Fig. 3e, f. Therefore, it can be concluded that that the proposed bridging technique can well control the wave reflection at the interface.

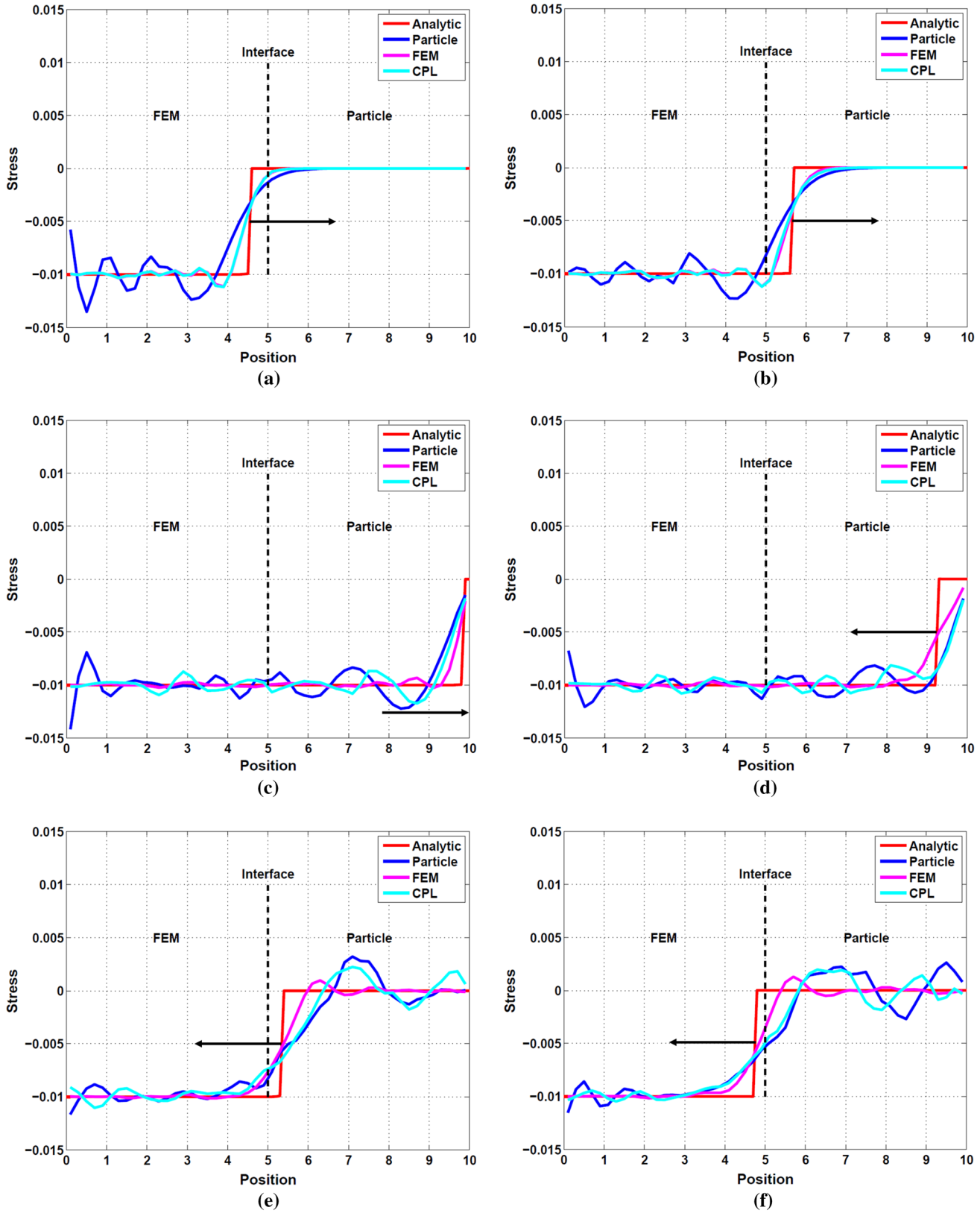

Fig. 3 Stress wave profiles at different time

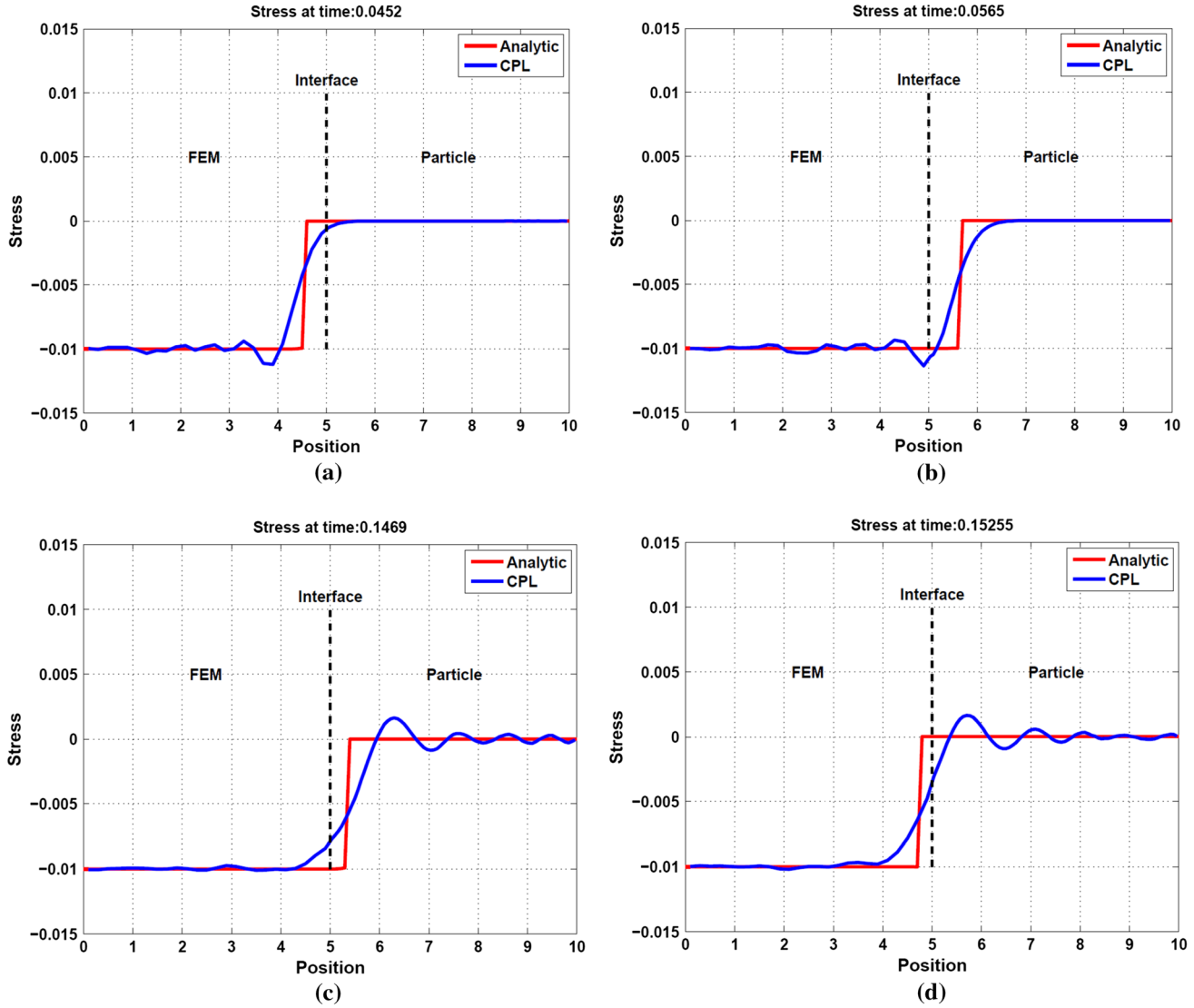

Fig. 4 Stress wave profiles at different times for the model with different nodal spacing in the FEM and particle domains

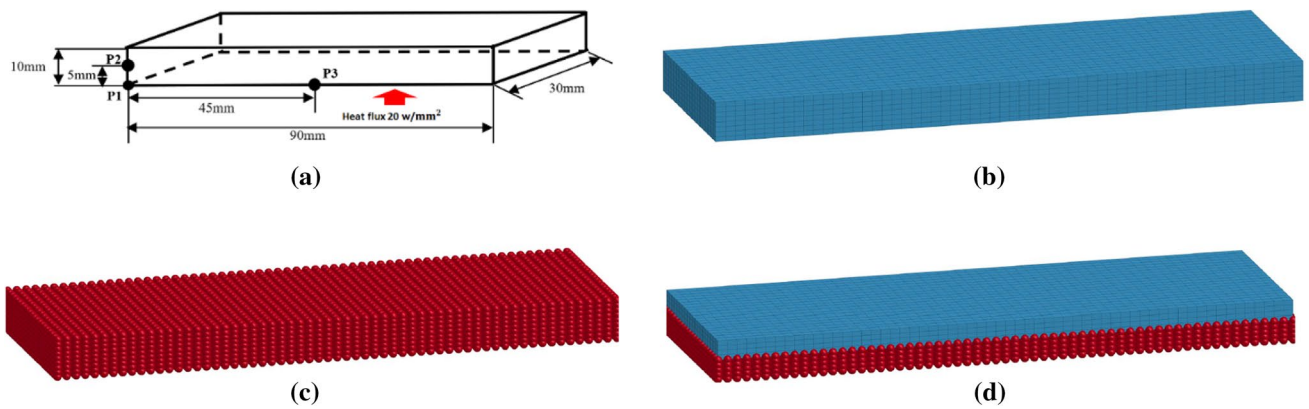

Fig. 5 Geometry and discretization of the aluminum plate. **a** Geometry; **b** FEM model; **c** particle model; **d** coupled model

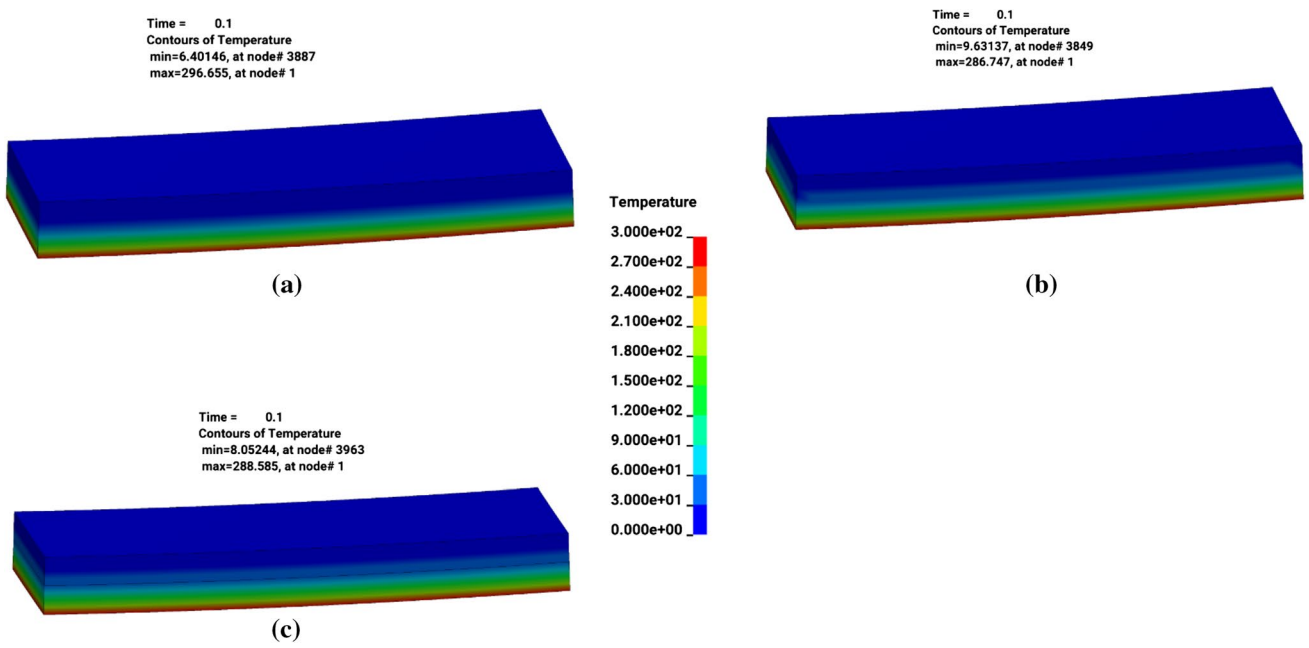

Fig. 6 Temperature contours at time t = 0.1 s: **a** FEM model; **b** particle model; **c** coupled model

In order to investigate the effect of the different nodal spacing in the FEM and particle domains to the wave reflection, the nodal spacing in the longitudinal direction in the particle domain is set as 1/3 of that used in Fig. 2, while the nodal spacing in FEM domain keeps unchanged, and the corresponding stress wave profiles at different times are shown in Fig. 4. It can be seen the wave reflection is still well controlled.

4.1.2 Heat conduction and thermal expansion

This example studies the coupled thermal mechanical response while the mechanical response is solely induced by pure thermal boundary conditions. An aluminum plate as shown in Fig. 5a has a size of 90 mm × 30 mm × 10 mm is used in the numerical test. The plate is free except a heat flux boundary with a constant flux of 20 W/mm^2 applied on its lower surface. The Young's modulus of the material is

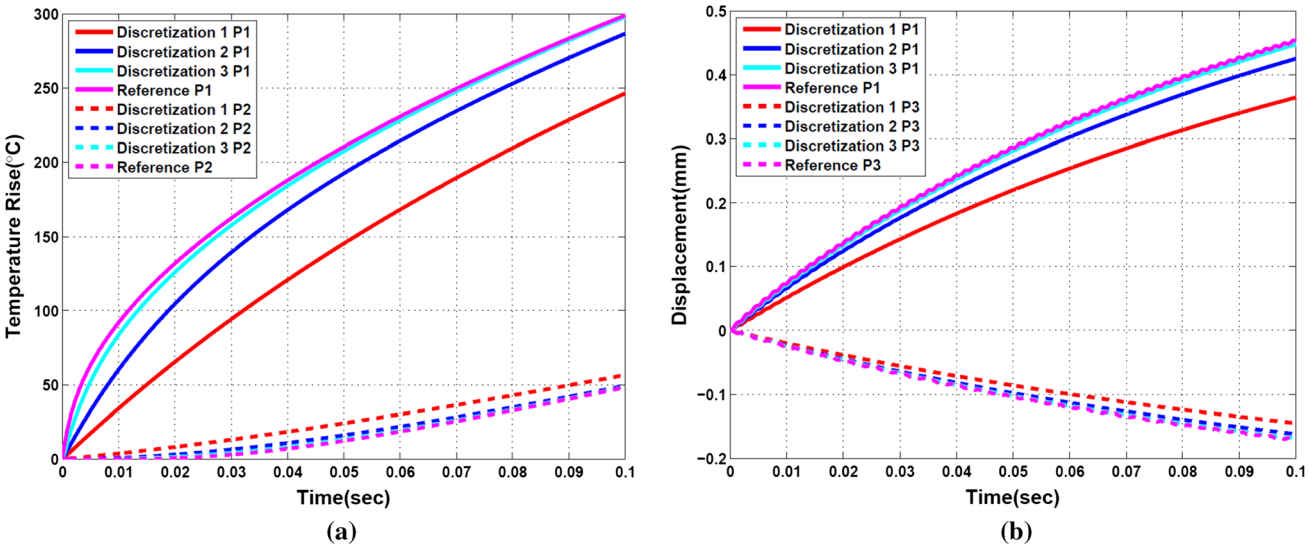

Fig. 7 Convergence study. **a** Temperature history; **b** Displacement history

70GPa, the Poisson's ratio is 0.3, and the density is 2700 kg/m^3. The thermal properties of material are: coefficient of thermal expansion 0.0000231, heat capacity 900 J/K, and heat conductivity 237 W/m–K. The initial temperature is 0 °C.

To study the effectiveness of the proposed particle formulation, three models are used in the simulations: (1) FEM model as shown in Fig. 5b; (2) particle model as shown in Fig. 5c; (3) coupled particle-FEM model as shown in Fig. 5d. In the coupled model, the upper half of the plate is modeled with FEM and the lower half is discretized by the particle method, and common nodes are used on the interface. Exactly same spatial discretization is used for all the three models, where the in-plane nodal distance is 1.25 mm, and the out-of-plane (thickness direction) nodal distance is 0.625 mm.

The temperature distributions obtained from the three models evaluated at time t = 0.1 s are plotted in Fig. 6. No significant difference is observed on the temperature fields obtained with the different models. Quantitatively, the maximum temperature rise from the particle model and the coupled model is 286.7 °C and 288.6 °C, respectively, which is about 3% different from the FEM result of 296.7 °C.

To study the convergence behavior of the present particle method in coupled thermal mechanical analysis, three discretizations are used: Discretization 1, the in-plane nodal distance is 2.5 mm, and the out-of-plane nodal distance is 1.25 mm; Discretization 2, the in-plane nodal distance is 1.25 mm, and the out-of-plane nodal distance is 0.625 mm; Discretization 3, the in-plane nodal distance is 0.625 mm, and the out-of-plane nodal distance is 0.3125 mm. The results from FEM with Discretization 3 is used as the reference. The temperature history is measured at locations P1 and P2 as shown in Fig. 5a. The displacement induced by thermal expansion is measured at locations P1 and P3 as shown in Fig. 5a.

Figure 7 shows the time histories of temperature and displacement at aforementioned designated locations obtained with the three different discretizations using the proposed particle formulation. Both solutions converge to the reference solution as discretization is refined. In addition, the accuracy of the particle method is very close to the finite element method provided that a same discretization is used (cf. Discretization 3 vs. Reference).

4.1.3 Taylor impact

The Taylor impact is a typical example to examine the accuracy of a numerical method in explicit dynamic analysis, which is used herein to study the coupled thermal

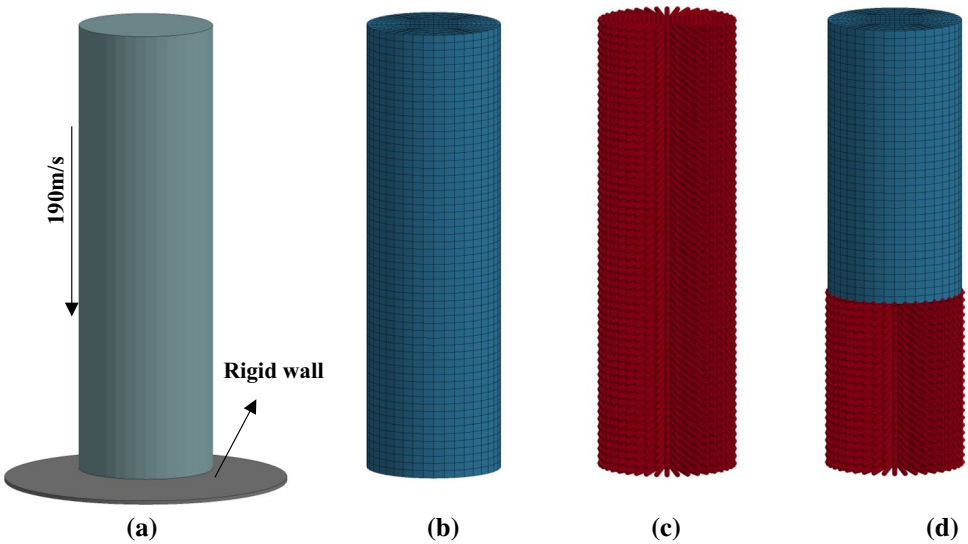

Fig. 8 Taylor impact: **a** Geometry and boundary conditions; **b** FEM model; **c** particle model; **d** coupled model

Table 1 Comparison of results in Taylor impact

	Initial geometry	Final geometry			
		Test	Particle model	Coupled model	FEM model
Diameter (mm)	7.6	13.5	14.6	14.5	14.8
Bulge (mm)	7.6	10.1	9.83	9.85	9.78
Length (mm)	25.4	16.2	16.3	16.3	16.4
$\bar{\Delta}$	–	–	0.038	0.035	0.047
Normalized CPU time	–	–	2.08	1.62	1.0

Table 2 Comparison of results in Taylor impact with different time step scale

	Time step scale factor		
	0.09	0.6	0.9
Diameter (mm)	14.6	14.6	14.5
Bulge (mm)	9.84	9.85	9.85
Length (mm)	16.4	16.3	16.3

mechanical response induced by pure mechanical boundary conditions. The thermal response in this case is solely induced by plastic strain energy and frictional sliding energy. The Johnson–Cook material law with thermal effect is used for the material modeling, and the material constants used in this simulation are taken from Ref. [40].

Figure 8 shows the geometry and FEM, particle and coupled particle-FEM models of the cylindrical bar. The bar impacts perpendicularly to the rigid surface at an initial impact velocity of 190 m/s. The initial length of the cylinder is $L_0 = 25.4$ mm and the initial diameter is $D_0 = 7.6$ mm. The shortest nodal spacing is 0.26 mm in the cross section and 0.42 mm in the longitudinal direction.

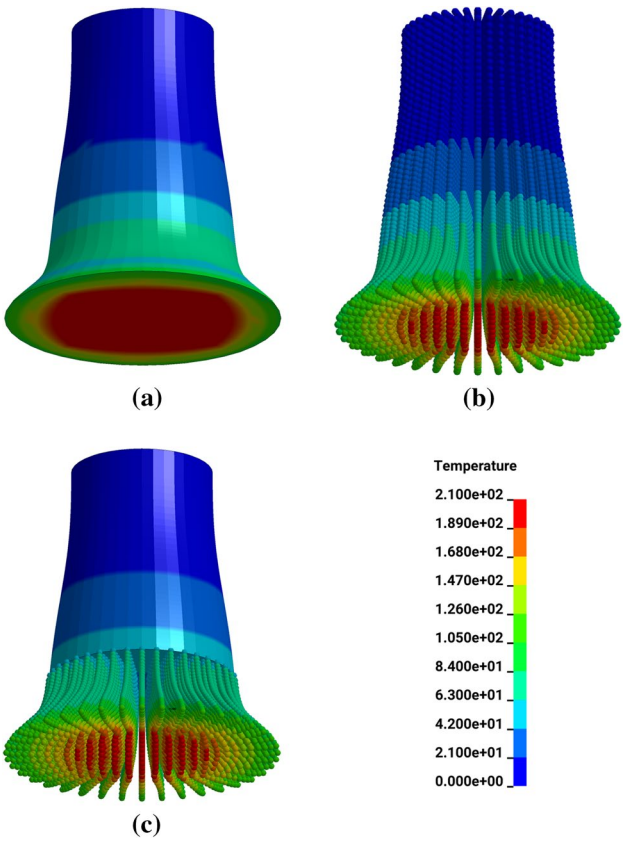

Fig. 9 Temperature fields at termination: **a** FEM model; **b** particle model; **c** coupled model

Table 1 summarizes the final geometries obtained from various methods. The experimental results are also included in the Table. An error measure introduced by Johnson and Holmquist [41] is calculated and listed in the Table, which defined as:

$$\bar{\Delta} = \frac{1}{3}\left[\frac{|\Delta L|}{L_{\text{exp}}} + \frac{|\Delta D|}{D_{\text{exp}}} + \frac{|\Delta W|}{W_{\text{exp}}}\right] \tag{42}$$

where $\Delta L = L_{\text{f}} - L_0$, $\Delta D = D_{\text{f}} - D_0$, $\Delta W = W_{\text{f}} - W_0$, and L_{exp}, D_{exp}, W_{exp} are the length, diameter and bulge measured in the experimental tests, while the bugle is measured at $0.2L_0$ to the bar bottom surface.

Table 1 shows that the numerical results are very close to the experimental test data, in general and the overall error is around 4% for all the methods. The normalized CPU time (normalized to that of FEM) for the particle model and coupled model is 2.08 and 1.62 respectively. The normalized CPU time also indicates that it does save some computational cost while the particle method is properly coupled with FEM.

As described in Sect. 3.2, the default time step scale factor for structural analysis is taken as 0.9. To investigate the sensitivity of the numerical results to the time step scale factor, various values are considered for comparison. In Table 2, the final deformations simulated with the coupled model are compared with the scale factors of 0.09, 0.6 and 0.9. No significant difference is observed on the final geometry including deformed bottom diameters, bugle and length. Therefore, the numerical performance of the present algorithm is insensitive to the structural time scale factor as long as it satisfies the CFL condition. On the other hand, it is highly recommended that a scale factor of 0.6 be used for a pure finite element analysis of this type of impact problem.

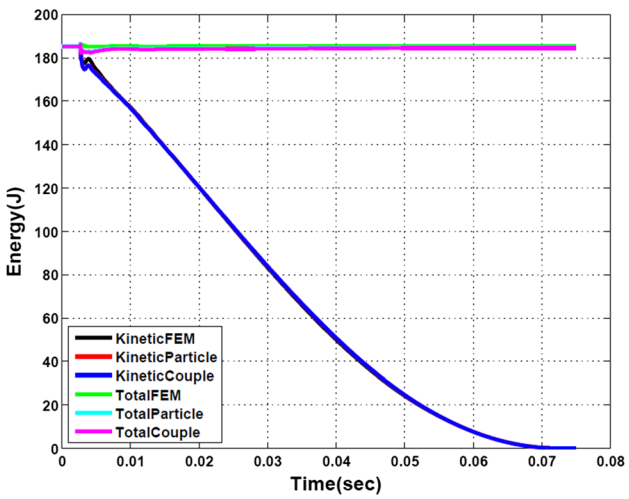

Fig. 10 Kinetic energy and total energy versus time

The scale factor should be further reduced if the impact velocity goes higher, which will dramatically increase the CPU time and it could even become more expensive than the particle method due to the different allowable time steps.

Figure 9 plots the temperature contours obtained with three models at termination. It is observed that the heat wave propagates smoothly from the impact contact surface to the free end of the bar, which indicates that the possible wave reflection at the FEM-particle interface in the coupled model is negligible. The temperature increment predicted by all the three models is very consistent as well. As mentioned earlier, the only heat source here is the plastic energy and frictional sliding energy while ignoring the heat conduction between the bar and the rigid surface. The heat convection and radiation are also not considered in the analysis because the impact time is very short.

Figure 10 shows the kinetic energy and total energy histories in the three analyses. The bar eventually stopped and thus the kinetic energy drops to zero. On the other hand, the only external energy source is the initial kinetic energy, therefore, the total energy is the initial kinetic energy. The figure shows that the loss of total energy is marginal, which indicates that the momentum consistent formulations satisfy the energy conservation laws.

4.2 Friction drilling

Non-traditional drilling and thread tapping processes such as friction drilling have become more and more popular in the automotive industry. Nevertheless, the majorities of the studies on the friction drilling are focused on the experiments [42–44]. Although few studies [43, 44] have been conducted using the finite element method and element erosion technique to simulate the large deformation and material failure problems in friction drilling application, several numerical issues remain to be resolved. For example, underestimated force and torque responses are often observed in finite element solution because of the loss of mass and linear momentum using the element erosion technique. The bushing also cannot be formed properly in the finite element simulation due to the eroding of elements. As a result, the finite element analysis of friction drilling application becomes problematic and parameter sensitive.

In this example, a friction drilling process is modeled using the proposed method. An AISI 304 stainless steel specimen is used in the friction drilling test. The steel plate has a diameter of 18 mm and thickness of 1.5 mm [42]. The geometry of the tool is shown in Fig. 11. The tool, which rotates at 3000 rpm and plunges at 100 mm/min in the test, is modeled by rigid material and meshed using tetrahedral elements. As can be seen in Fig. 11, the metal workpiece is discretized with three models: (a) model 1, using 10,560 elements for FEM; (2) mode 2, using 4767 particles for the particle method in the central area within a diameter 6.4 mm and 6720 elements for FEM for the rest of the area; (c) using 7567 particles for the particle method in the central area within a diameter of 10 mm and 4320 elements for FEM for the remaining area. The shortest nodal distance in the central area is about 0.25 mm. The perimeter of the workpiece is clamped.

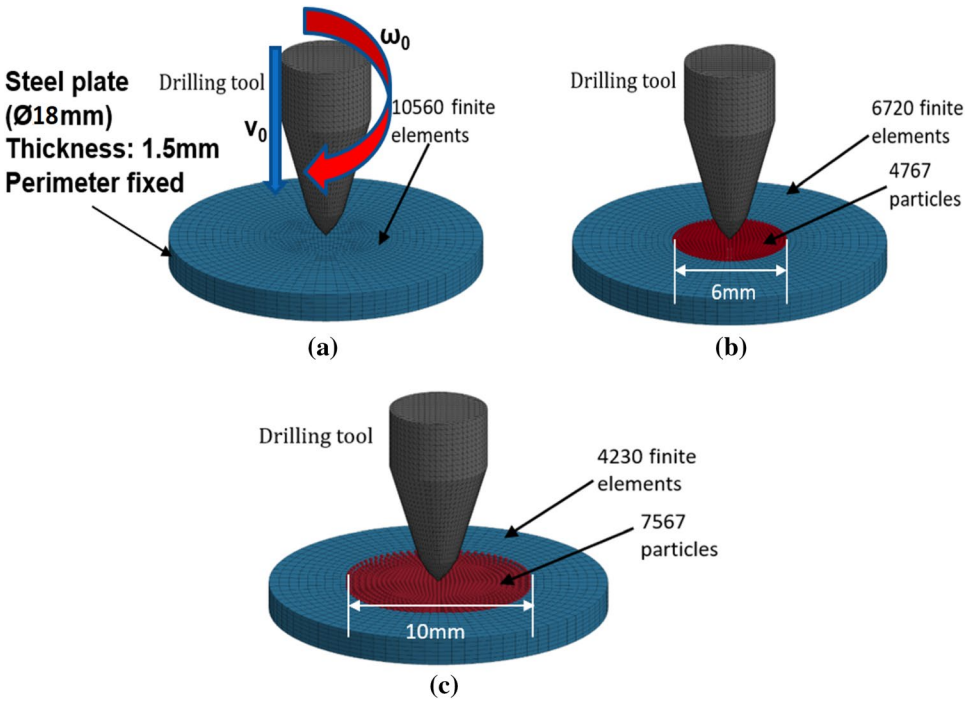

Fig. 11 Discretization: **a** Finite element model. **b** Coupled mode 1. **c** coupled model 2

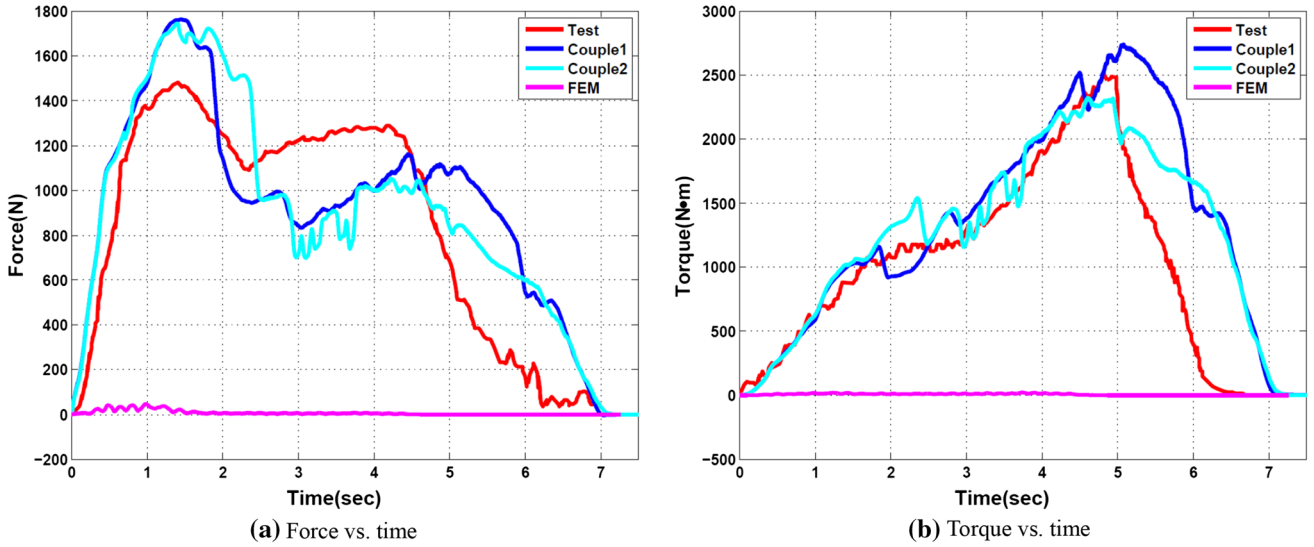

(a) Force vs. time **(b)** Torque vs. time

Fig. 12 Responses of friction drilling: **a** Thrust force, **b** Torque

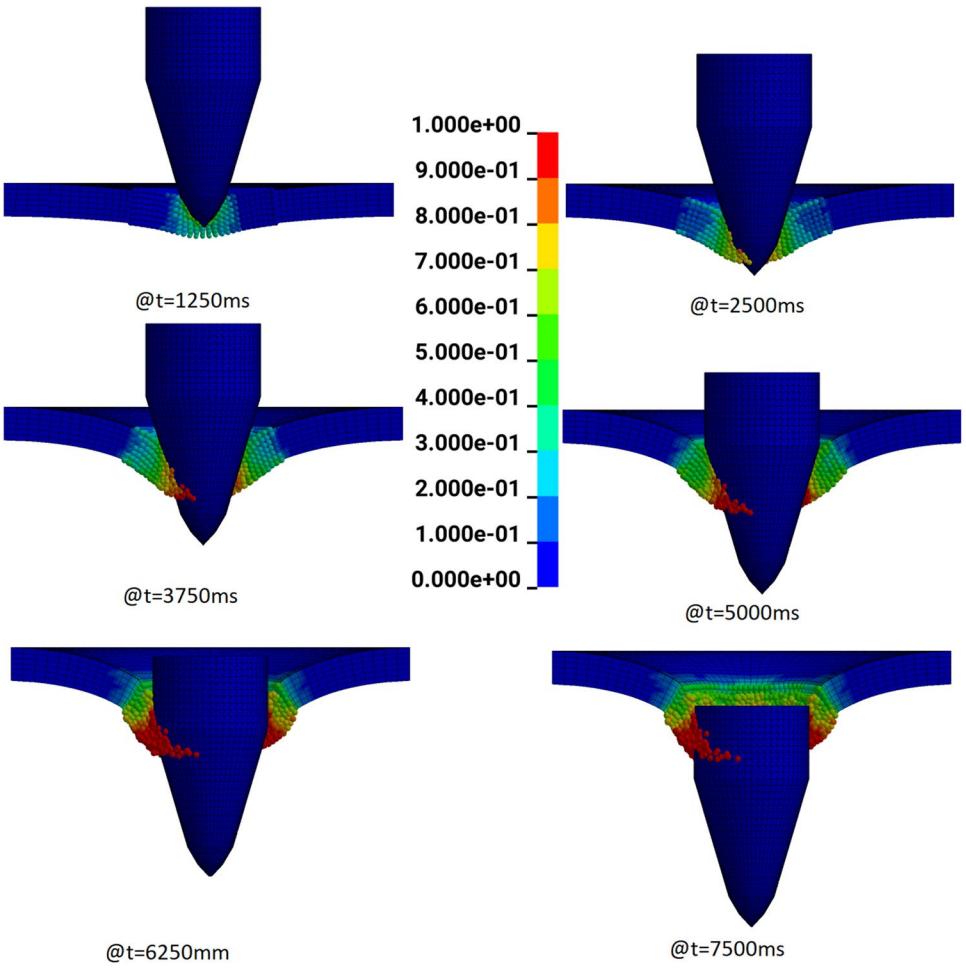

Fig. 13 Friction drilling: effective plastic strain distribution

The stress flow in the AISI 304 steel is modeled by the Johnson–Cook material law [45] with parameters of: A = 205 MPa, B = 602.5 MPa, C = 0.08, m = 1.09, n = 0.622. The failure behavior of the steel is handled by the bond failure mechanism introduced for the smoothed particle Galerkin method [29, 33] rather than the Johnson–Cook damage

law, and the effective plastic strain for bond failure [33] is set to 0.4, which is also used as the triggering criterion for element erosion in the finite element analysis. According to efunda (www.efunda.com), the Young's modulus of the workpiece is set to 193 GPa. The thermal properties of the AISI stainless steel are: coefficient of thermal expansion 0.0000184, heat capacity C_p 500 J/kg-K, and thermal conductivity κ 16.2 W/m–K. The coefficient of friction (COF) between the tool and the workpiece is set to 0.35 for the node-to-surface contact algorithm in the numerical analysis. The fraction of heat generation β in the frictional contact is taken to be 0.5. The Taylor-Quinney [35] coefficient η of 0.9 is considered in Eq. (2). The interfacial heat transfer between the tool and the workpiece is neglected. The heat convection and radiation are ignored as well.

The comparison of the thrust force and torque is presented in Fig. 12a, b, respectively. As shown in Fig. 12a, b both the force and torque are significantly underestimated by finite element method with element erosion technique, which is attributed to the considerable mass, momentum and energy loss when element erosion occurs, while the force and torque responses obtained from the two coupled models capture the basic profiles of the experimental data nicely. The difference between the results from the coupled models is not significant, which indicates that the numerical results are not sensitive to the size of the zone that is modeled by the particle method, as long as it is big enough to cover the zone where material failure occurs. More physical modeling of the material, the frictional contact, the heat transfer between the tool and the workpiece, and the heat dissipation etc. should help to capture the response more accurately, which is not the focus of this research.

Figure 13 shows the evolution of the effective plastic strain in the workpiece using model 2, while only half is plotted. Red color indicates effective plastic strain level of 1.0 or more. It is worthwhile to emphasize that the creation

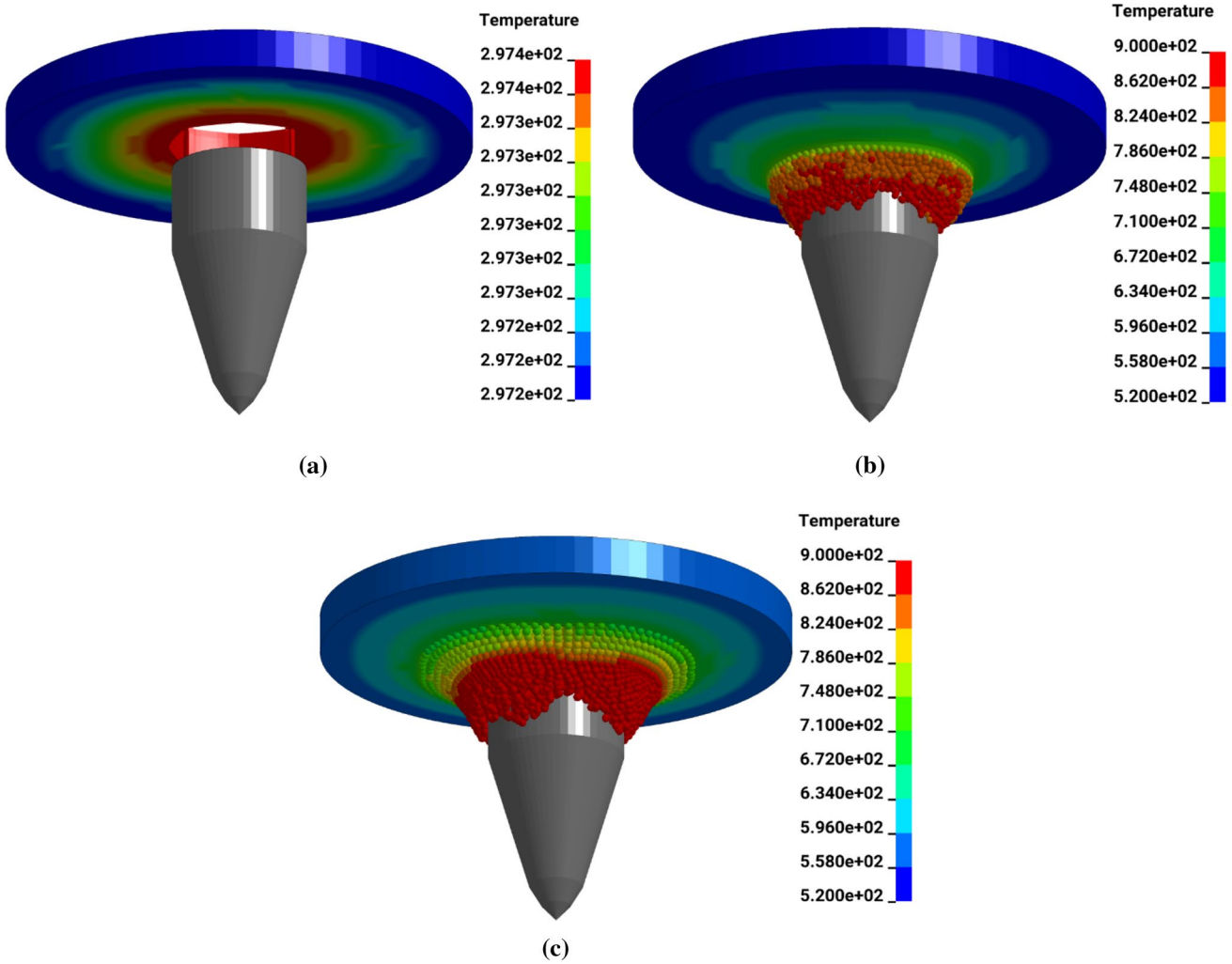

Fig. 14 Friction drilling—temperature field in workpiece. **a** FEM model; **b** coupled model 1; **c** coupled model 2

of the bushing is one of the major purposes of this type of manufacturing process so that it can be used in the future connection/jointing process. The present method captures the bushing nicely.

Figure 14 demonstrates the temperature distribution in the workpiece at termination of the analysis. The simulation results from both coupled models are very close to the measured temperature on the upper side of the disc at the contact zone which was reported at 842 K [42], while the temperature predicted by the FEM model is significantly lower because the energy to be converted to heat is lost due to the element erosion when failure occurs.

5 Conclusions

The main difficulty in finite element modeling of friction drilling process consists in dealing with high levels of deformations involving in the complex material flow due to frictional heating and material separation at the bushing forming stage. Despite the enormous progress achieved lately in computational mechanics, the development of an advanced numerical tool for the robust and accurate friction drilling simulation continues to be nowadays an emerging need for industry.

In this study, a momentum-consistent stabilization algorithm to the Lagrangian particle method is introduced for simulating the friction drilling application. Several benchmark tests have verified that the present method is suitable for the three-dimensional thermo-mechanical analysis. The results in the last example suggest that the present method can produce the desired physics in the forming of a bushing. The results also reveal that the present method can generate reasonable force and torque responses compared with the experimental data. The existing literature has not been able to demonstrate similar results. The extension of this method to other thermo-mechanical problems that consider complex multi-physics behaviors such as phase transformation and phase change will be the focus of our future development.

Acknowledgements The authors wish to thank Dr. John O. Hallquist of LSTC for his support to this research. The support from Ford Motor Company is also gratefully acknowledged.

Appendix 1: Proof of linear and angular momentum consistency

In the present particle method, the shape function $\phi_I^a(\boldsymbol{X}_J)$ is constructed by using the moving least squares (MLS) [46] formulation in the current configuration, and the linear basis $p^{\mathrm{T}}(\boldsymbol{x}) = [1, x, y, z]$ is used. Because MLS approximation can reproduce any polynomial used in the basis, we have

$$\sum_{I\in Z_I} \phi_I^a(\boldsymbol{X}_J)\boldsymbol{x}_I = \boldsymbol{x}_J \tag{43}$$

which is used in the following derivation. For detailed proof of the reproducing condition in Eq. (43) can be found in [47].

Linear momentum consistency in the velocity smoothing procedure

In the smoothing procedure at the beginning of every time step it can be shown that the sum of the nodal momentums $\sum_{I\in Z_I} \boldsymbol{P}_I$ equals to that of unsmoothed nodal momentums $\sum_{I\in Z_I} \hat{\boldsymbol{P}}_I$, that is

$$\begin{aligned}\sum_{I\in Z_I} \boldsymbol{P}_I &= \sum_{I\in Z_I} m_I\dot{\boldsymbol{u}}_I \\ &= \sum_{I\in Z_I}\sum_{J\in Z_I} \hat{m}_J\phi_I^a(\boldsymbol{X}_J)\hat{\dot{\boldsymbol{u}}}_J \\ &= \sum_{J\in Z_I}\sum_{I\in Z_I} \hat{m}_J\phi_I^a(\boldsymbol{X}_J)\hat{\dot{\boldsymbol{u}}}_J \\ &= \sum_{J\in Z_I} \hat{m}_J\hat{\dot{\boldsymbol{u}}}_J \\ &= \sum_{J\in Z_I} \hat{\boldsymbol{P}}_J\end{aligned} \tag{44}$$

Angular momentum consistency in the velocity smoothing procedure

It can also be verified that the sum of nodal angular momentums $\sum_{I\in Z_I} \boldsymbol{L}_I$ equals to that of unsmoothed nodal momentums $\sum_{I\in Z_I} \hat{\boldsymbol{L}}_I$, that is

$$\begin{aligned}\sum_{I\in Z_I} \boldsymbol{L}_I &= \sum_{I\in Z_I} \boldsymbol{x}_I \times m_I\dot{\boldsymbol{u}}_I \\ &= \sum_{I\in Z_I}\sum_{J\in Z_I} \boldsymbol{x}_I \times m_J\phi_I^a(\boldsymbol{X}_J)\hat{\dot{\boldsymbol{u}}}_J \\ &= \sum_{J\in Z_I}\sum_{I\in Z_I} \left(\boldsymbol{x}_I\phi_I^a(\boldsymbol{X}_J)\right) \times \hat{m}_J\hat{\dot{\boldsymbol{u}}}_J \\ &= \sum_{J\in Z_I} \boldsymbol{x}_J \times \hat{m}_J\hat{\dot{\boldsymbol{u}}}_J \\ &= \sum_{J\in Z_I} \hat{\boldsymbol{L}}_J\end{aligned} \tag{45}$$

Linear momentum consistency in the velocity updating procedure

In the velocity updating procedure at the end of each time step, it can be verified that sum of the updated unsmoothed nodal momentums $\sum_{I\in Z_I}\hat{\boldsymbol{P}}_I^{n+1}$ equals to that of updated nodal momentums $\sum_{I\in Z_I}\boldsymbol{P}_I^{*,n+1/2}$, that is

$$\begin{aligned}\sum_{J\in Z_I}\hat{\boldsymbol{P}}_J^{n+1/2} &= \sum_{J\in Z_I}\hat{m}_J\left(\hat{\dot{\boldsymbol{u}}}_J^{n-1/2}+\Delta t_n^u\sum_{I\in Z_I}\hat{m}_J\phi_I^a(\boldsymbol{X}_J)\ddot{\boldsymbol{u}}_I^n\right)\\ &= \sum_{J\in Z_I}\hat{m}_J\hat{\dot{\boldsymbol{u}}}_J^{n-1/2}+\Delta t_n^u\sum_{J\in Z_I}\left(\sum_{I\in Z_I}\hat{m}_J\phi_I^a(\boldsymbol{X}_J)\ddot{\boldsymbol{u}}_I^n\right)\\ &= \sum_{I\in Z_I}\hat{\boldsymbol{P}}_I^{n-1/2}+\Delta t_n^u\sum_{I\in Z_I}\sum_{J\in Z_I}\hat{m}_J\phi_I^a(\boldsymbol{X}_J)\ddot{\boldsymbol{u}}_I^n\\ &= \sum_{I\in Z_I}\boldsymbol{P}_I^{n-1/2}+\Delta t_n^u\sum_{I\in Z_I}m_I\ddot{\boldsymbol{u}}_I^n\\ &= \sum_{I\in Z_I}m_I\dot{\boldsymbol{u}}_I^n+\Delta t_n^u\sum_{I\in Z_I}m_I\ddot{\boldsymbol{u}}_I^n\\ &= \sum_{I\in Z_I}\boldsymbol{P}_I^{*,n+1/2}\end{aligned} \tag{46}$$

Angular momentum consistency in the velocity updating procedure

The sum of updated unsmoothed angular momentums $\sum_{I\in Z_I}\hat{\boldsymbol{L}}_I^{n+1/2}$ in the velocity updating procedure is

$$\begin{aligned}\sum_{I\in Z_I}\hat{\boldsymbol{L}}_I^{n+1/2} &= \sum_{I\in Z_I}\boldsymbol{x}_I^n\times\hat{m}_I\left(\hat{\dot{\boldsymbol{u}}}_I^{n-1/2}+\Delta t_n^u\sum_{J\in Z_I}\phi_J^a(\boldsymbol{X}_I)\ddot{\boldsymbol{u}}_J^n\right)\\ &= \sum_{I\in Z_I}\boldsymbol{x}_I^n\times\hat{m}_I\hat{\dot{\boldsymbol{u}}}_I^{n-1/2}+\Delta t_n^u\sum_{I\in Z_I}\boldsymbol{x}_I^n\times\hat{m}_I\sum_{J\in Z_I}\phi_J^a(\boldsymbol{X}_I)\ddot{\boldsymbol{u}}_J^n\\ &= \sum_{I\in Z_I}\hat{\boldsymbol{L}}_I^{n-1/2}+\Delta t_n^u\sum_{I\in Z_I}\boldsymbol{x}_I^n\times\hat{m}_I\sum_{J\in Z_I}\phi_J^a(\boldsymbol{X}_I)\ddot{\boldsymbol{u}}_J^n\end{aligned}$$

The sum of updated angular momentums $\sum_{I\in Z_I}\boldsymbol{L}_I^{*,n+1/2}$ in the velocity updating procedure is

$$\begin{aligned}\sum_{I\in Z_I}\boldsymbol{L}_I^{*,n+1/2} &= \sum_{I\in Z_I}\boldsymbol{x}_I^n\times m_I\left(\dot{\boldsymbol{u}}_I^{n-1/2}+\Delta t_n^u\ddot{\boldsymbol{u}}_I^n\right)\\ &= \sum_{I\in Z_I}\boldsymbol{x}_I^n\times m_I\dot{\boldsymbol{u}}_I^{n-1/2}+\Delta t_n^u\sum_{I\in Z_I}\boldsymbol{x}_I^n\times m_I\ddot{\boldsymbol{u}}_I^n\\ &= \sum_{I\in Z_I}\boldsymbol{L}_I^{n-1/2}+\Delta t_n^u\sum_{I\in Z_I}\boldsymbol{x}_I^n\times m_I\ddot{\boldsymbol{u}}_I^n\end{aligned} \tag{47}$$

It's known that $\sum_{I\in Z_I}\hat{\boldsymbol{L}}_I^{n-1/2}=\sum_{I\in Z_I}\boldsymbol{L}_I^{n-1/2}$, we have

$$\begin{aligned}&\sum_{I\in Z_I}\hat{\boldsymbol{L}}_I^{n+1/2}-\sum_{I\in Z_I}\boldsymbol{L}_I^{*,n+1/2}\\ &\quad=\Delta t_n^u\sum_{I\in Z_I}\boldsymbol{x}_n(\boldsymbol{X}_I)\times\left(\hat{m}_I\sum_{J\in Z_I}\phi_J^a(\boldsymbol{X}_I)\ddot{\boldsymbol{u}}_J^n-m_I\ddot{\boldsymbol{u}}_I^n\right)\end{aligned}$$

Subsequently,

$$\sum_{I\in Z_I}\hat{\boldsymbol{L}}_I^{n+1/2}-\sum_{I\in Z_I}\boldsymbol{L}_I^{*,n+1/2}\approx 0\text{ as }\Delta t_n^u\to 0$$

Appendix 2: Coupling with FEM

In general, the efficiency of particle method is lower than the finite element method in the small deformation analysis. On the other hand, the particle method could be more effective than finite element method in large deformation analysis, thus it is beneficial to apply the particle method in the large deformation region, while the finite element method is employed in the small deformation region. As a result, a bridging scheme that couples the two numerical methods will need to be developed.

Consider a 1D case as shown in Fig. 15 for the illustration of the bridging scheme. The sharing node that defines the interface in this 1D problem provides a kinematical connection between the FEM part and the part made of Lagrangian particles. The sharing node can be further divided into the FEM node and the particle from the present method. Due to continuity, both the FEM nodes and the present particles should have the same acceleration, velocity, displacement and temperature at the interface. Following the derivation in Sect. 3.1, the nodal momentum of the sharing node at $\boldsymbol{X}_I$ of Fig. 15 is the sum of the momentum from the contribution of the FEM node and the Lagrangian particles. That is,

$$\boldsymbol{P}_I^{\text{Sharing}}=\boldsymbol{P}_I^{\text{FEM}}+\boldsymbol{P}_I^{\text{Particle}}=\hat{m}_I^{\text{FEM}}\hat{\boldsymbol{u}}_I+\sum_{J\in Z_I}\hat{m}_J\phi_I^a(\boldsymbol{X}_J)\hat{\boldsymbol{u}}_J \tag{48}$$

The mass of the sharing node at $\boldsymbol{X}_I$ is

$$m_I^{\text{Sharing}}=m_I^{\text{FEM}}+m_I^{\text{Particle}}=\hat{m}_I^{\text{FEM}}+\sum_{J\in Z_I}\hat{m}_J\phi_I^a(\boldsymbol{X}_J) \tag{49}$$

Subsequently, the velocity at the sharing node becomes

$$\begin{aligned}\dot{\boldsymbol{u}}_I^{\text{Sharing}} &= \boldsymbol{P}_I^{\text{Sharing}}/m_I^{\text{Sharing}}\\ &= \left(\hat{m}_I^{\text{FEM}}\hat{\boldsymbol{u}}_I+\sum_{J\in Z_I}\hat{m}_J\phi_I^a(\boldsymbol{X}_J)\hat{\boldsymbol{u}}_J\right)\Big/\left(\hat{m}_I^{\text{FEM}}+\sum_{J\in Z_I}\hat{m}_J\phi_I^a(\boldsymbol{X}_J)\right)\end{aligned} \tag{50}$$

The stresses and strains of the Lagrangian particles and FEM integration points are updated in a standard way.

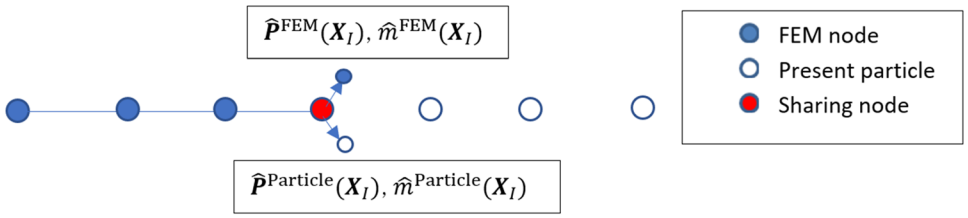

Fig. 15 Illustration of the bridging scheme

Finally, the integration of the mechanical weak form of Eq. (3) is composed of FEM part and the Lagrangian particle part using the DNI scheme to yield

$$\boldsymbol{M}^{\mathrm{sum}}\ddot{\boldsymbol{U}} = \boldsymbol{F}^{\mathrm{ext}} + \boldsymbol{F}^{\mathrm{c}} - \boldsymbol{F}^{\mathrm{int,sum}} \tag{51}$$

where $\boldsymbol{M}_{\mathrm{sum}} = \boldsymbol{M}_{\mathrm{FEM}} + \boldsymbol{M}_{\mathrm{Particle}}$

After the nodal displacement increment is evaluated, the updating of displacement fields is based on three different groups of nodes:

1. For the nodes in the FEM part but not belong to the sharing nodes, the standard FEM is used.

$$\boldsymbol{u}_I^{h,\mathrm{FEM},n+1} = \boldsymbol{u}_I^{n+1} \tag{52}$$

2. For the nodes in the Lagrangian particle part, but not belong to the sharing nodes, the particle approximation is used.

$$\boldsymbol{u}_I^{h,\mathrm{Particle},n+1} = \sum_{J\in Z_I} \phi_J^a(\boldsymbol{X}_I)\boldsymbol{u}_J^{n+1} \tag{53}$$

3. For the sharing node, the momentum-consistent algorithm is used to yield

$$\boldsymbol{u}_I^{h,\mathrm{Sharing},n+1} = \frac{\left(\hat{m}_I^{\mathrm{FEM}}\boldsymbol{u}_I^{h,\mathrm{FEM},n+1} + \hat{m}_I^{\mathrm{Particle}}(\boldsymbol{X}_I)\boldsymbol{u}_I^{h,\mathrm{Particle},n+1}\right)}{\left(\hat{m}_I^{\mathrm{FEM}} + \hat{m}_I^{\mathrm{Particle}}\right)} \tag{54}$$

At the end of each time step, the particle velocities should be updated. They are

1. For the nodes in the Lagrangian particle part, but not belonging to the sharing nodes, the unsmoothed nodal velocities are updated using the Eq. (22).
2. For the sharing nodes, the momentum-consistent algorithm is used again, that is

$$\hat{\boldsymbol{u}}_I^{\mathrm{Sharing},n+1/2} = \hat{\boldsymbol{u}}_I^{\mathrm{Sharing},n-1/2} + \Delta t_n^u \hat{\boldsymbol{u}}_I^{\mathrm{Sharing},n} \tag{55}$$

where,

$$\hat{\boldsymbol{u}}_I^{\mathrm{Sharing},n} = \frac{\hat{m}_I^{\mathrm{FEM}}\hat{\boldsymbol{u}}_I^{\mathrm{FEM},n} + \hat{m}_I^{\mathrm{Particle}}\hat{\boldsymbol{u}}_I^{\mathrm{Particle},n}}{\hat{m}_I^{\mathrm{FEM}} + \hat{m}_I^{\mathrm{Particle}}} \tag{56}$$

The bridging technique developed for the mechanical analysis is also suitable for the thermal analysis and thus it is not repeated here.

References

1. Miller SF, Shih AJ, Blau PJ (2005) Microstructural alterations associated with friction drilling of steel, aluminum, and titanium. J Mater Eng Perform 15:647–653
2. Miller SF, Shih AJ (2007) Thermo-mechanical finite element modeling of the friction drilling process. J Manuf Sci Eng 129:531–538
3. Belytschko T, Liu WK, Moran B, Elkhodary KI (2014) Nonlinear finite elements for continua and structures, 2nd edn. Wiley, London
4. Raju BP, Swamy MK (2012) Finite element simulation of a friction drilling procedure using Deform-3D. Int J Eng Res Technol 2:716–721
5. Gopichand A, Brahmam MV, Bhanuprakash D (2014) Numerical simulation and analysis of friction drilling process for aluminum alloy using Ansys. Int J Eng Res Technol 3:602–607
6. Buffa G, Hua J, Shivpuri R, Fratini L (2006) A continuum based fem model for friction stir welding—model development. Mater Sci Eng, A 419:389–396
7. Meyghani B, Awang MB, Emamian SS, Mohd Nor MKB, Pedapati SR (2017) A comparison of different finite element methods in the thermal analysis of friction stir welding (FSW). Metals 7(10):450
8. Chen JS, Pan C, Wu CT, Liu WK (1996) Reproducing kernel particle methods for large deformation analysis of non-linear structures. Comput Methods Appl Mech Eng 139:195–227
9. Rabczuk T, Belytschko T (2004) Cracking particles: a simplified meshfree method for arbitrary evolving cracks. Int J Numer Methods Eng 61:2316–2343
10. Simkins DC, Li S (2006) Meshfree simulation of thermo-mechanical ductile fracture. Comput Mech 38:235–249
11. Li S, Liu WK (2004) Meshfree particle method. Springer, Berlin
12. Wang DD, Chen JS (2004) Locking free stabilized conforming nodal integration for meshfree Mindlin-Reissner plate formulation. Comput Methods Appl Mech Eng 193:1065–1083
13. Gingold RA, Monaghan JJ (1977) Smoothed particle hydrodynamics—theory and application to non-spherical stars. Mon Not R Astron Soc 181:375–389
14. Lucy LB (1977) A numerical approach to the testing of the fission hypothesis. Astron J 82:1013–1024
15. Libersky LD, Petschek AG (1990) Smooth particle hydrodynamics with strength of materials. Lect Notes Phys 395:248–257
16. Shadloo MS, Oger G, Touzé DL (2016) Smoothed particle hydrodynamics method for fluid flows, towards industrial applications: motivations, current state, and challenges. Comput Fluid 136:11–34
17. Swegle W, Hicks DL, Attaway SW (1995) Smoothed particle hydrodynamics stability analysis. Comput Mech 116:123–134

18. Belytschko T, Guo Y, Liu WK, Xiao SP (2000) A unified stability analysis of meshless particle methods. Int J Numer Methods Eng 48:1359–1400
19. Wu CT, Ma N, Takada K, Okada H (2016) A meshfree continuous-discontinuous approach for the ductile fracture modeling in explicit dynamics analysis. Comput Mech 58:391–409
20. Rabczuk T, Belytschko T, Xiao SP (2004) Stable particle methods based on Lagrangian kernels. Comput Methods Appl Mech Eng 193:1035–1063
21. Dyka CT, Randles PW, Ingel RP (1997) Stress points for tension instability in SPH. Int J Numer Methods Eng 40:2325–2341
22. Beissel S, Belytschko T (1996) Nodal integration of the element-free Galerkin method. Comput Methods Appl Mech Eng 139:49–74
23. Wu CT, Koishi M, Hu W (2016) A displacement smoothing induced strain gradient stabilization for the meshfree Galerkin nodal integration method. Comput Mech 56:19–37
24. Hillman M, Chen JS (2016) An accelerated, convergent, and stable nodal integration in Galerkin meshfree methods for linear and nonlinear mechanics. Int J Numer Methods Eng 107:603–630
25. Chen JS, Wu CT, Yoon S, You Y (2001) A stabilized conforming nodal integration for Galerkin Meshfree methods. Int J Numer Methods Eng 50:435–466
26. Hillman M, Chen JS, Chi SW (2014) Stabilized and variationally consistent nodal integration for meshfree modeling of impact problems. Comput Particle Mech 1:245–256
27. Guan PC, Chen JS, Wu Y, Tang H, Gaidos J, Hofstetter K, Alsaleh M (2009) Semi-Lagrangian reproducing kernel formulation and application to modeling earth moving operations. Mech Mater 41:670–683
28. Wu CT, Chi SW, Koishi M, Wu Y (2016) Strain gradient stabilization with dual stress points for the meshfree nodal integration method in inelastic analysis. Int J Numer Methods Eng 107:3–30
29. Wu CT, Wu Y, Crawford JE, Magallanes JM (2017) Three-dimensional concrete impact and penetration simulations using the smoothed particle Galerkin method. Int J Impact Eng 106:1–17
30. Chen JS, Zhang X, Belytschko T (2014) An implicit gradient model by a reproducing kernel strain regularization in strain localization problems. Comput Methods Appl Mech Eng 193:2827–2844
31. Wu CT, Wu Y, Liu Z, Wang D (2018) A stable and convergent Lagrangian particle method with multiple nodal stress points for large strain and material failure analyses in manufacturing processes. Finite Elem Anal Des 146:96–106
32. Silling SA, Askari E (2005) A meshfree method based on the peridynamic model of solid mechanics. Comput Struct 83:1526–1535
33. Wu CT, Bui TQ, Wu YC, Luo TL, Wang M, Liao CC, Chen PY, Lai YS (2018) Numerical and experimental validation of a particle Gakerkin method for metal grinding simulation. Comput Mech 61(365):383
34. Felippa CA, Park KC (1980) Staggered transient analysis procedures for coupled dynamic systems. Comput Methods Appl Mech Eng 26:61–112
35. Hughes TJR (2000) The finite element method. Prentice-Hall, Englewood Cliffs
36. Hallquist JO (2006) LS-DYNA® keyword user's manual. Livermore Software Technology Corporation, Livermore
37. Liu WK, Chen Y (1995) Wavelet and multiple scale reproducing kernel particle methods. Int J Numer Methods Fluid Dyn 21:901–931
38. Liu WK, Uras RA, Chen Y (1997) Enrichment of the finite element method with reproducing kernel particle method. J Appl Mech 135:143–166
39. Belytschko T, Organ D, Krongauz Y (1995) A coupled finite element-element-free Galerkin method. Comput Mech 17:186–195
40. Sulsky D, Schreyer HL (1996) Axisymmetric form of the material point method with application to upsetting and Taylor impact problems. Comput Methods Appl Mech Eng 139:409–429
41. Johnson GR, Holmquist TJ (1988) Evaluation of Cylinder-impact test data for constitutive model constants. J Appl Phys 64:3901–3910
42. Krasauskas P, Kilikevičius S, Česnavičius R, Pačenga D (2014) Experimental analysis and numerical simulation of the stainless AISI 304 steel friction drilling process. Mechanika 20:590–595
43. Chow HM, Lee SM, Yang LD (2018) Machining characteristic study of friction drilling on AISI 304 stainless steel. J Mater Process Technol 207:180–186
44. Lee SM, Chow HM, Huang FY, Yan BH (2009) Friction drilling of austenitic stainless steel by uncoated and PVD AlCrN- and TiAlN-coated tungsten carbide tools. Int J Mach Tools Manuf 49:81–88
45. Johnson GR, Cook WH (1983) A constitutive model and data for metals subjected to large strains, high strain rates, and high temperatures. In: Proceedings of the 7th international symposium on ballistics (1983), pp 541–547, The Hague, Netherlands
46. Belytschko T, Lu YY, Gu L (1994) Element-free Galerkin Methods. Int J Numer Methods Eng 37:229–256
47. Liu WK, Jun S, Li S, Adee J, Belytschko T (1995) Reproducing kernel particle methods for structural dynamics. Int J Numer Methods Eng 38:1655–1679